# DeepGEM-EGF: A Bayesian strategy for joint estimates of source-time functions and empirical Green's functions

Théa Ragon<sup>1,2</sup>, Angela F. Gao<sup>3</sup>, Zachary E. Ross<sup>1</sup>

<sup>1</sup>Seismological Laboratory, California Institute of Technology, Pasadena, CA, USA.

<sup>2</sup>now at CNRS, Univ. Grenoble Alpes, IRD, ISTerre, Grenoble, France

<sup>3</sup>Computing and Mathematical Sciences Department, California Institute of Technology, Pasadena, CA, USA

This is a non-peer-reviewed manuscript preprinted in EarthArXiv

# **Key Points:**

11

12

15

- We propose a new Bayesian framework for estimating source time functions and optimizing one or several prior Empirical Green's Functions (EGFs)
- DeepGEM-EGF accounts for epistemic uncertainties and efficiently discriminates source parameters given approximations made in the forward model
- DeepGEM-EGF robustly estimates complex source time functions with high-frequency content and exhibits limited sensitivity to prior EGF(s) selection

Corresponding author: Théa Ragon, thea.ragon@univ-grenoble-alpes.fr

Abstract

17

18

19

21

22

23

24

25

26

27

29

30

31

32

33

34

35

37

39

40

41

44

45

46

48

49

51

52

53

55

56

57

58

59

60

61

65

An earthquake record is the convolution of source radiation, path propagation and site effects, and instrument response. Isolating the source component requires solving an ill-posed inverse problem. Whether the instability of inferred source parameters arises from varying properties of the source, or from approximations we introduce in solving the problem, remains an open question. Such approximations often derive from limited knowledge of the forward problem. The Empirical Green's function (EGF) approach offers a partial remedy, by approximating the forward response of large events using the records of smaller events. The choice of the « best » small event drastically influences the properties estimated for the larger earthquake. Discriminating variability in source properties from epistemic uncertainties, stemming from the forward problem or other modeling assumptions, requires us to reliably account for, and propagate, any bias or trade-off introduced in the problem. We propose a Bayesian inversion framework that aims at providing reliable and probabilistic estimates of source parameters (here, for the source-time function or STF), and their posterior uncertainty, in the time domain. We jointly solve for the best EGF using one or a few small events as prior EGF. Our approach expands on DeepGEM, an unsupervised generalized expectation-maximization framework for tomography (A. F. Gao et al., 2021). We demonstrate, with toy models and various applications to mainshocks of Mw ranging from  $\sim$ 4 to 6.3, the potential of DeepGEM-EGF to disentangle the variability of the seismic source from biases introduced by modeling assumptions.

# Plain Language Summary

Our understanding of earthquakes is based on the analysis of earthquake waveforms recorded at the surface of the Earth. These waveforms contain two types of information that we try to discriminate from each other: earthquake properties and characteristics of the ground the waves propagate through. But the earthquake properties we estimate are difficult to interpret: it remains unclear whether their variability is inherent to the earthquake nature, or derives from the approximations used in our analysis. One common approach offers a partial remedy, in using a nearby small earthquake to better constrain a larger one: the two earthquakes share similar ground characteristics in their recorded waveforms. But the results depend heavily on which small earthquake is chosen. We introduce a new deep learning framework that probabilistically estimates earthquake properties in the time domain, and related uncertainties. Instead of using a single small nearby earthquake, our approach can combine information from several small earthquakes. We demonstrate the potential of the framework using simple models and and several applications to real earthquakes of variable magnitude. Our method proves efficient at disentangling earthquake properties from uncertainties caused by the analysis process.

#### 1 Introduction

Our understanding of how earthquakes start, grow, and stop resides in our ability to build physical models from observed source and rupture properties. Variations in rupture pattern, velocity and directivity, radiated energy and stress drop are examined to provide constraints on fault zone processes (e.g., Kanamori & Brodsky, 2004). The variability of source parameters has practical implications for hazard assessment as it impacts ground shaking predictions (e.g., Anderson & Brune, 1999; Pavic et al., 2000; Boore, 2003; Cotton et al., 2013; A. S. Baltay et al., 2013; Oth et al., 2017; Gerstenberger et al., 2020). Source (and slip) scaling currently dictates how we relate observations, physical processes and hazard (e.g., Aki, 1996; Cotton et al., 2013; Cocco et al., 2016; Lambert et al., 2021). Yet, our insight on whether large and small earthquakes strictly share similar properties (Aki, 1967), or if their physics diverge, remains nuanced because of the puzzling instability of the source parameters we infer (e.g., Shearer et al., 2006; Viesca & Garagash, 2015; Lin &

Lapusta, 2018; Hardebeck, 2020; Abercrombie, 2021; Bindi et al., 2023; Abercrombie, Baltay, et al., 2025; Abercrombie, Chen, et al., 2025).

67

68

69

70

71

72

73

74

76

77

78

79

80

83

84

85

87

88

89

90

92

93

96

97

99

100

101

102

103

104

105

106

107

108

109

110

111

112

113

115

116

117

118

119

An earthquake record is the convolution of source radiation, path propagation and site effects, and instrument response. Isolating the source component requires solving an ill-posed inverse problem; however there are questions regarding whether above-mentioned instabilities arise from the source, or from approximations we introduce in the problem. Since the pioneering work of Hartzell (1978), the Empirical Green's function (EGF) approach is a widely used assumption that spares us the need to model a costly forward problem (e.g., Frankel & Kanamori, 1983; Mueller, 1985; Frankel et al., 1986; Hutchings & Wu, 1990; Dreger, 1994; Ihmlé, 1996; Courboulex et al., 1996; Hough, 1997). Assuming that the only difference in the recordings of two similar and co-located earthquakes is due to their respective rupture, then an event small enough to have an impulsive source can be used as a Green's function for a larger one. However, the choice of the "best" EGF remains a large source of epistemic uncertainties, because of discrepancies in focal mechanism, non-impulsivity of the small event, relative hypocentral distance, finite bandwidth, and noise contamination (e.g., Viegas et al., 2010; Kane et al., 2011, 2013; Abercrombie, 2015, and references therein). Using several potential events (e.g., Hough, 1997; Abercrombie et al., 2017) or averaging over a dense cluster of events and stations (generalized spectral decomposition, e.g., Andrews, 1986; Prieto et al., 2006; Shearer et al., 2006; Bindi et al., 2009; Trugman & Shearer, 2017) are good palliative approaches, but they fail at accounting for the actual impact of approximations in the forward problem on our understanding of source physics.

Approximations we introduce in the blind (i.e., when the forward problem is unknown) source deconvolution problem also derive from data selection, non-physically justified priors and any modeling assumptions. Such approximations could regroup (and are not limited to) any a priori choices made for: data pre-processing and collection (choice of frequency bandwidth, stations selection and coverage, local path effects or attenuation; e.g., Abercrombie, 2015; Abercrombie et al., 2017; Shearer et al., 2019; Chu et al., 2024). regularization of the inverse problem (ad-hoc selection of water-level threshold value or other regularization parameters, see references below), any assumption for the source or rupture model (superposition of a fixed-number of simple peaks in the time-domain, or the use of simple circular rupture models in the frequency-domain, prior definition of fixed source durations, etc; e.g., Kaneko & Shearer, 2015). Abercrombie, Chen, et al. (2025) show that while different EGF approaches, using similar data, yield consistent results for simple sources, their outcomes diverge significantly for more complex ones. Consequently, properties derived a posteriori from estimated parameters (such as total rupture duration, number of subevents, directivity, stress drop) are likely to be affected by artifacts rising from epistemic uncertainties. A particularly interesting illustration is the second moment formulation, which relies on estimated ASTFs duration (e.g., G. Backus & Mulcahy, 1976; G. E. Backus, 1977; McGuire et al., 2001). Inferred characteristic rupture properties often suffer from strong instabilities, that can be related to approximations, either introduced in the formulation, or deriving from uncertainties in ASTFs duration (e.g., McGuire & Kaneko, 2018; Fan & McGuire, 2018; Neely et al., 2019). We therefore need new approaches that can robustly discriminate source complexity from artifacts induced by epistemic uncertainties, particularly those linked to EGF selection.

Discriminating variability in source properties from epistemic uncertainties requires us to reliably account for, and propagate, any uncertainty and trade-off (as already suggested by many authors, e.g., Abercrombie & Rice, 2005; Prieto et al., 2006; Shearer et al., 2019; Trugman, 2022). To do so, spectral ratio analyses have seen recent progress towards Bayesian inversion frameworks, facilitated by the small number of parameters involved (e.g., Godano et al., 2015; Garcia-Aristizabal et al., 2016; Van Houtte & Denolle, 2018; Supino et al., 2019; Törnman et al., 2021; Trugman, 2022). Frequency-domain analyses, whether they be generalized decompositions or spectral divisions, are usually more

popular, for computational speed and the reduced number of parameters. In contrast, time-domain analyses could reduce the posterior variability of inferred source parameters (Courboulex et al., 2016) while improving constraints on a few properties such as directivity (e.g., Boatwright, 1984; McGuire, 2004; Trugman, 2022). Yet, time-domain analyses are, so far, limited to deterministic optimization approaches (e.g., Vallée, 2004; Plourde & Bostock, 2017; Gallegos & Xie, 2020) that could hinder our ability to monitor and assess variability of the source.

120

121

124

125

126

127

129

130

131

133

134

135

137

138

141

142

143

145

149

150

151

152

153

154

155

156

157

158

159

162

163

164

167

168

Here, we propose a time-domain Bayesian inversion framework that aims to provide reliable and probabilistic estimates of source parameters and their uncertainty. To do so, we consider the EGF assumption as a potential cause of epistemic uncertainties and discard any oversimplification of the problem. The objective of this paper is to introduce our approach and validate its ability to perform for a variety of applications.

We first apply our method on toy models to test the performance of DeepGEM-EGF for the robust inference of both STFs and EGFs under harsh assumptions: incorrect priors, poor candidate EGFs, etc. The idea behind those tests is to define under which conditions our approach would fail, and how we can interpret those failures. We then investigate several case study to benchmark our results with synthetic tests and existing analyses, and to showcase the benefits of DeepGEM-EGF. Our goal is to assess our approach for typical applications, with a range of moderate to large Mw and various data. We select three well-studied, well-recorded events as target earthquakes, which we know have well-recorded, small, co-located earthquakes that could be used as appropriate EGFs. We first analyze apparent STFs for an Mw 5.2 event that occurred near Borrego-Springs, CA, USA, in 2016, because this event has a single candidate EGF of very good quality (Ross et al., 2017). We then focus on the 2016-2019 Cahuilla swarm, CA, USA: we exploit the multiple candidate EGFs surrounding the largest Mw 4.4 event to inspect the effect of prior EGF selection on our estimates. Finally, we test our approach against a larger event: the 2009 Mw 6.3 l'Aquila earthquake, Italy. A summary of the tests and test cases we present in this manuscript is available in Table 1. These case studies demonstrate the potential of DeepGEM-EGF to improve estimates of complex STFs, and in turn deepen our understanding of the source of earthquakes, and in particular of its variability.

# 2 DeepGEM-EGF: Generalized Expectation-Maximization for blind deconvolution

The approach we propose, DeepGEM-EGF, is twofold: we explore the solution space for any probable source-time function (STF) using one or more candidate EGFs, while considering these EGFs to be a good, but slightly incorrect, prior that needs updating (Fig. 1).

The inverse problem that we are trying to solve can be written as  $\mathbf{d} = G_{\theta}(\mathbf{m})$ ;  $\mathbf{d}$  being the observed data,  $\mathbf{m}$  the parameters of the inverse problem (the STF), G the forward problem (i.e. convolution with the EGFs), and  $\theta$  the parameters of G representing the EGFs. Solving for both  $\mathbf{m}$  and  $\theta$  is an ill-posed problem. We want to estimate the posterior uncertainty on the STF, but generally already have good prior knowledge on the forward problem as we have selected one or multiple EGFs. We therefore choose to estimate the posterior probability  $p(\mathbf{m}|\mathbf{d},\theta)$  on  $\mathbf{m}$  while solving for one best estimate of  $\theta$  that maximizes the log likelihood  $p(\theta|\mathbf{d})$  considering all of the potential solutions for  $\mathbf{m}$ .

To do so, we follow an approach derived from DeepGEM (A. F. Gao et al., 2021), a variational Bayesian Expectation-Maximization (EM) framework that can be used to solve for the parameters of both an inverse problem and a forward model in an unsupervised manner. DeepGEM was initially designed for blind tomography (where the forward problem, or earthquakes locations, is unkown), but has also proven to be effective for a simple blind image deconvolution problem (blind meaning that the convolution kernel is

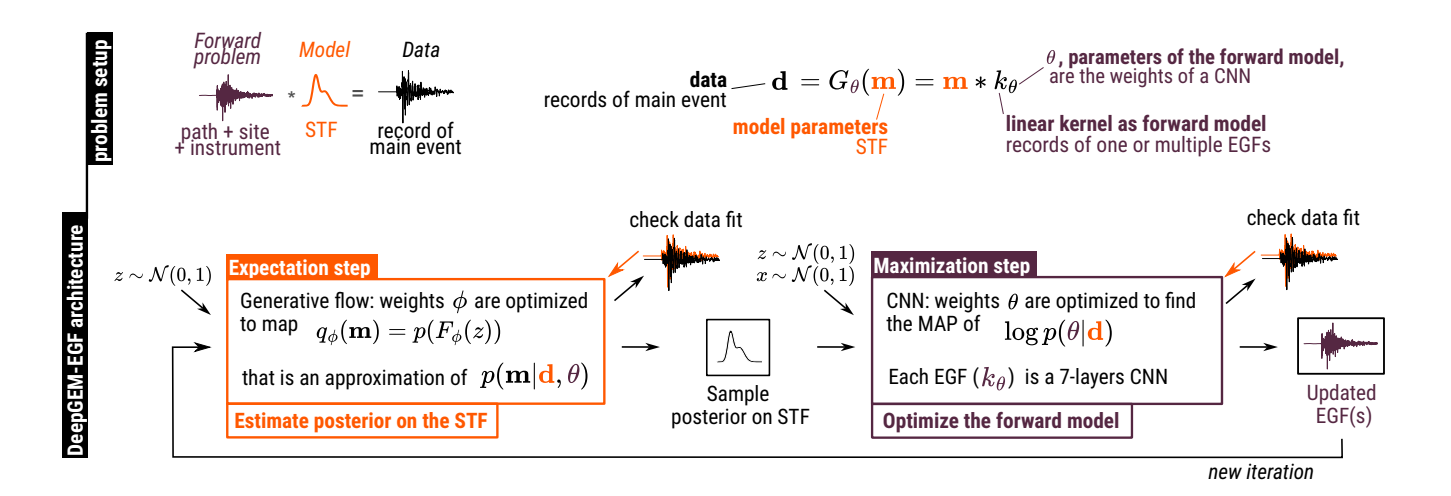


Figure 1. Cartoon representing the principle and architecture of DeepGEM-EGF.

unknown; A. F. Gao et al., 2021). Similarly, our EM-like approach iterates between two steps; (1) an E-step that learns an approximation to the posterior distribution of  $\mathbf{m}$  given the fixed forward model parameters  $\theta^{(i-1)}$  inferred at the previous iteration i-1; and (2) an M-step that solves for  $\theta^{(i)}$  considering the fixed parameters of the inverse problem solved in the prior E-step. We present here the main characteristics, and modifications from the initial framework, of DeepGEM-EGF.

#### 2.1 Expectation step: solving for the Source-Time Function

The expectation step (i.e E-step) aims to approximate the posterior distribution of our target STF  $\mathbf{m}$  knowing the data  $\mathbf{d}$ . The E-step is based on a normalizing flow-based generative model, whose architecture is derived from the one of Deep Probabilistic Imaging (DPI, Sun & Bouman, 2021; Sun et al., 2022). We infer the posterior distribution  $q_{\phi}(\mathbf{m})$  using variational inference where the class of normalizing flow-based neural networks defines our variational distribution. We optimize the network to generate samples of  $q_{\phi}(\mathbf{m})$  that fit our data: we then evaluate an expectation of  $q_{\phi}(\mathbf{m})$ .

We parameterize  $q_{\phi}(\mathbf{m})$  with a normalizing flow  $F_{\phi}$  such that  $q_{\phi}(\mathbf{m}) = p(F_{\phi}(z))$ .  $F_{\phi}$  allows us to map a complicated distribution  $p(F_{\phi}(z))$  as a composition of L invertible transformations  $F_{\phi_L} \circ F_{\phi_{L-1}} \circ \dots \circ F_{\phi_1}$  applied to Gaussian samples z where L is the number of layers for the generative flow. At the i-th E-step, we optimize the weights  $\phi^{(i)}$  of  $F_{\phi^{(i)}}$  that best approximates our posterior distribution  $p(\mathbf{m}|\mathbf{d},\theta^{(i-1)})$  through the following objective:

$$\phi^{(i)} = \arg\min_{\phi} KL \left( q_{\phi}(\mathbf{m}) \parallel p(\mathbf{m}|\mathbf{d}, \theta^{(i-1)}) \right)$$

$$\approx \arg\min_{\phi} \frac{1}{N} \sum_{n=1}^{N} \left[ -\log p(\mathbf{d} \mid \theta^{(i-1)}, \mathbf{m}_{n}) - \log p(\mathbf{m}_{n}) + \beta \log q_{\phi}(\mathbf{m}_{n}) \right],$$
(1)

for  $\mathbf{m}_n = F_{\phi}(z_n)$ ,  $z_n \sim \mathcal{N}(0,1)$ , a batch size of N, the prior on the STF  $\log p(\mathbf{m})$ , the data likelihood  $\log p(\mathbf{d}|\mathbf{m}, \theta^{i-1})$ , and KL denotes the Kullback-Leibler divergence.  $\beta$  is an additional hyperparameter proposed in DPI to control the entropy of the generative model's posterior samples; see full derivations in Sun and Bouman (2021). We use a Real-NVP network (Dinh et al., 2016) for  $F_{\phi}$  with L=32 affine coupling layers. We use Adam (Kingma & Ba, 2014) as the optimizer with a batch size of 1024.

We define a realistic prior over the normalized amplitude of the STF as  $p(\mathbf{m}) \sim \mathcal{N}(\overline{\mathbf{m}}, \sigma_m)$ . By default,  $\overline{\mathbf{m}}$  is a Gaussian-shaped STF with a  $\sigma_m$  of 5% in amplitude. The default Gaussian-shaped  $\overline{\mathbf{m}}$  is centered on half of the preset STF length, and has a width equal to 10% of the total preset STF duration. By default, the weight of this prior is small and its nature has a very limited impact on the results. In practice, for synthetic tests, the shape of the prior STF (symmetric, e.g. Brune-like, or asymmetric) does not influence the estimates, even if the STF used to calculate the synthetic data does have a different shape (Figs 2,3). The assumed  $\sigma_m$  has a larger impact, in particular on the posterior standard deviation, as it conditions the exploration of the solution space.

Because the weight of the prior STF is small, we augment  $p(\mathbf{m})$  with a few specific constraints. We want the STF to be close to zero on its boundaries, and we enforce sparsity with a  $\ell_1$  norm. With sparsity regularization, we avoid overestimating the complexity of the STF due to noise and data over-fitting, while allowing for sharp changes in the solution. We also impose a total variation regularization. Default hyperparameters (weights for the specific constraints) were empirically chosen by inspecting the loss and the fit to synthetic tests on a grid search.

# 2.2 Maximization step: optimizing the EGFs for the forward model

The maximization step (i.e. M-step) relies on estimates of the approximate posterior  $q_{\phi}(\mathbf{m})$  from the preceding E-step to update  $\theta$ , the parameters of the unknown forward model, from the initially assumed set of EGF(s). We define  $G_{\theta}$  as the convolution between model parameters  $\mathbf{m}$  and a linear kernel  $k_{\theta}$  of parameters  $\theta$ . The kernel is a deep network consisting in multiple convolution layers without non-linear activation, as proposed in Bell-Kligler et al. (2019) and successfully applied in A. F. Gao et al. (2021):

$$G_{\theta}(\mathbf{m}) = \mathbf{m} * k_{\theta} = \mathbf{m} * \frac{\theta_1 * \theta_2 * \dots * \theta_K}{||\theta_1 * \theta_2 * \dots * \theta_K||_{\infty}},$$
(2)

for a K-layer network. During the *i*-th M-step, we optimize the weights  $\theta^{(i)}$  to find the maximum a posteriori (MAP) of the posterior distribution of parameters  $\theta$  knowing the

$$\theta^{(i)} = \arg \max_{\theta} \log p(\theta \mid \mathbf{d})$$

$$\approx \arg \max_{\theta} \left[ \frac{1}{N} \sum_{n=1}^{N} \left[ \log p\left(\mathbf{d} \mid \theta, \mathbf{m}_{n}\right) \right] + \log p(\theta) \right],$$
for  $\mathbf{m}_{n} = F_{\phi^{(i)}}\left(\mathbf{z}_{n}\right), \, \mathbf{z}_{n} \sim \mathcal{N}(0, 1).$ 
(3)

Conceptually, each kernel  $k_{\theta}$  is an EGF that consists in a convolution network.  $\theta$  are the weights of the convolution network, and therefore do not have a physical relationship with the EGFs: they are updated to optimize the fit to the data. We use K=7 convolution layers to parameterize  $G_{\theta}$ . We use Adam as the optimizer.

As we already have a good guess for our forward model, we use a prior  $\log p(\theta)$  that encourages the forward model to stay close to the initially assumed set of EGF(s). We define  $\log p(\theta)$  as a weighted sum of mean absolute error  $(\mathcal{L}_{\phi})$ ,  $\ell_2$ -norm, and dynamic time warping norm  $(\mathcal{L}_{DTW})$  between the updated and initial EGF(s)  $k_{\theta_0}$ :

$$\log p(\theta) = -\lambda_{\phi} \sum_{H} \frac{\mathcal{L}_{\phi}}{|k_{\theta_0} - k_{\theta^{(i)}}|} - \lambda_2 \sum_{H} (k_{\theta_0} - k_{\theta^{(i)}})^2 - \lambda_{DTW} DTW_{0.1}(k_{\theta^{(i)}}, k_{\theta_0}), \quad (4)$$
with  $H$  the length of  $k_{\theta^{(i)}}$ .

When considering multiple candidate EGFs, we parameterize  $k_{\theta}$  as an array of independent deep networks. During the *i*-th M-step and for each EGF e, weights  $\theta_e^{(i)}$  are

optimized. We augment  $\log p(\theta)$  with a prior  $\mathcal{L}_{\text{multi}}$  that encourages the inferred EGFs to converge towards a single EGF  $k_{\theta_{\text{best}}^{(i)}}$  that minimizes  $\alpha_e^{(i)}$ , the misfit between data and predictions:

$$\log p(\theta) = -\mathcal{L}_{\phi} - \ell_2 - \mathcal{L}_{DTW} - \lambda_{\text{multi}} \sum_{e} \alpha_e^{(i)} \sum_{e}^{H} (k_{\theta_e^{(i)}} - k_{\theta_{\text{best}}^{(i)}})^2, \tag{5}$$

with 
$$k_{\theta_{\text{best}}^{(i)}} = \arg\min_{e} \alpha_e^{(i)} \propto \sum_{e}^{H} (\mathbf{m}^{(i)} * k_{\theta_e^{(i)}} - \mathbf{d})^2$$
 (6)

Additionally, MSE loss for each EGF can be weighted with a user-defined parameter that can reflect the quality of each a priori selected EGF. Weights  $\lambda_{\phi}, \lambda_{2}, \lambda_{DTW}$  and  $\lambda_{\text{multi}}$  were empirically chosen with a grid search on synthetic tests.

214

215

216

217

219

220

221

	STF duration (s)	M main event	M EGF	nbr of EGFs	Filter frequency (Hz)	Sampling rate (Hz)	Wave arrivals	Figures
Toy models	2 – 10	$\sim \!\! 4 - 6.5$	3	1 to 4	no filter	10	P, S, all	Fig. 2, Figs. S1, S2
Borrego Springs, CA - main: Mw 5.2, EGF: ML 3.37								
Synthetic tests	~1.2-1.5	~5	~3	1	0.1-30	50 (data at 100)	P	Fig. 3, Fig. S3
Real data	~1.2	$\sim$ 5	~3	1	0.1-30	50 (data at 100)	Р	Fig. 4, Figs. S3, S4
Cahuilla, CA - main: Mw 4.4, EGF: multiple $M\sim 2-2.5$								
Synthetic tests	$\sim 0.5$	$\sim 4$	$\sim 2$	1 to 8	0.1-40	20 or 40 (data at 40)	P, S	Fig. 5, Fig. S5
Real data	$\sim 0.5$	$\sim 4$	~2	1 to 8	0.1-40	20 or 40 (data at 40)	P, S	Figs. 6,7, Figs. S6, S7
L'Aquila, IT - main: Mw 6.3, EGF: multiple 3.8 <mw<4.9< td=""></mw<4.9<>								
Synthetic tests	12	~6	~4	1	0.1-2	6 (data at 25)	P, S	Fig. 8, Figs. S8, S9
Real data	12	Mw 6.3	~4	1	0.1-2	6 (data at 25)	P, S	Fig. 9, Figs. S10 to S12

 $\textbf{Table 1.} \quad \text{Summary of design choices for various tests. Details are in Supplementary Material.}$ 

# 3 Benchmark on toy models

We conducted numerous preliminary tests, covering a wide range of data frequencies and ASTFs durations, that we do not detail in this manuscript. These were used to constrain, select, and fine-tune hyper-parameters and priors, as well as to assess their influence (see Suppl. Mat. Tables S1 and S2 for full parameter lists). A few hyper-parameters do have a notable impact on the results. The weight on the misfit between data and predictions

(data\_sigma) is critical and controls the quality of the inversion. To a lesser extent, the assumed standard deviation on the prior STF (stf0\_sigma,  $\sigma_m$ ) influences the exploration of the solution space and therefore the posterior standard deviation. In our default setup, and in the results presented in this paper, the weight on the prior STF (stf0\_weight) is low, and therefore the nature of the assumed prior STF has a negligible impact. However, increasing this weight amplifies the influence of incorrect priors, introducing biases proportional to its value (or its ratio to the data misfit weight). Most other hyper-parameters, with a much milder effect, are a function of data\_sigma. Finally, network parameters such as learning rates and the number of epochs or sub-epochs will control convergence behavior.

For a few tests, we compare DeepGEM-EGF results with non-blind deconvolution approaches; a multitaper deconvolution approach (e.g., Thomson, 1982; Percival & Walden, 1993; Prieto et al., 2009) and an iterative projected Landweber approach (Bertero et al., 1997). We chose both these algorithms as they are well-documented and have been used extensively. These approaches require a few additional assumptions or processing steps that are detailed in Suppl. Mat. S2.

In this section, we investigate the ability of DeepGEM-EGF to robustly infer both STFs and EGFs when assumed EGFs are poor candidates. We build toy models, based on fully synthetic waveforms, of increasing difficulty, meaning of increasing discrepancies between actual GFs and assumed EGFs. With these toy models, our objective is to define under which conditions our approach would fail, and how to interpret those failures. The discrepancies we analyze can affect source properties (absolute location, focal mechanism, duration), medium (velocity model) or recordings (noise). These toy models are unrealistic, in the sense that we do not trade-off the frequency range of the data, the Mw, and the duration of the source; and all amplitudes are normalized. We do not investigate the effect of attenuation or site effects, even if such effects are included via changes in velocity models.

We first perform series of toy models with synthetic waveforms calculated at 10 Hz, using all of the arrivals (P, S and coda), 1D velocity models (with 5 to 8 layers of varying Vp, Vs and  $\rho$  and increasing attenuation with depth; details in Suppl. Mat. S3, Tables S4-S6). The target STF consists of a stack of 3 to 10 pulses parameterized as Gaussian functions with randomly varying width and heights, and a duration ranging from 2 to 10 s. Double-couple source properties (location, depth, moment tensor) for the main event (the largest) are random. Source properties for synthetic EGFs randomly vary away from the properties of the main event. Kagan angle (Kagan, 1991) between moment tensors of the source and assumed EGFs vary between 5 and 40°. We add white noise at 10 Hz, with a peak signal to noise ratio ranging from 0-10%, to waveforms of both the main event and EGFs. We do not filter or decimate the waveforms.

We show the results of a subset of these tests, for increasingly challenging scenarios, in Fig. 2. We also plot, for each test, the ability of DeepGEM-EGF to correctly estimate target STFs against the distance between target and prior EGF in Suppl. Mat. Fig. S1. In general, target STFs are well recovered, including the width, amplitude and start and end times of multiple peaks of various durations (tests (a) to (d), Fig. 2). This remains true even when prior EGFs are moderately incorrect, meaning that cross-correlation or L2 distances between prior and assumed EGFs are low or large, respectively (Suppl. Mat. Fig. S1, tests (c) to (e)). In most cases, predicted waveforms fit the data well. Estimated EGF waveforms are usually close to the target ones, even when the prior is off, without overfitting the additional noise. STF fits from a multitaper approach are outperformed, even for very simple tests (e.g., Suppl. Mat. Fig. S1, right). The choice of the prior EGF has a strong impact on the quality of the results: the larger the discrepancy between the prior and target EGF waveforms, the larger the misfit between inferred and target STFs (Suppl. Mat. Fig. S1). DeepGEM-EGF converges well even if the source of the prior EGF

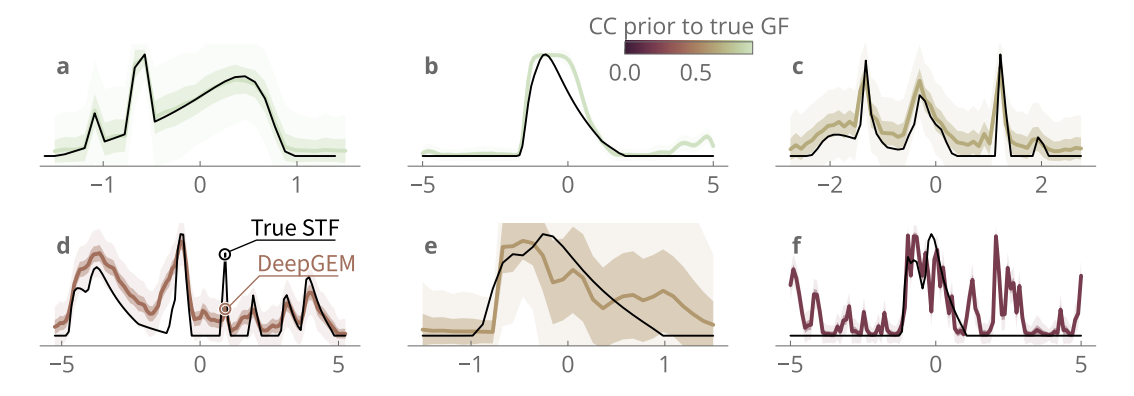


Figure 2. A set of increasingly challenging scenarios for toy models designed with fully synthetic waveforms. Inferred (colored) and target (black) Source-Time Functions (STFs) are shown, the mean of the STFs being colored by the peak cross-correlation value between prior and target Empirical Green's functions; the standard deviation is shaded ( $1\sigma$  darker,  $3\sigma$  lighter). Tests (c) to (f) are particularly challenging: the prior EGF is moderately to highly dissimilar from the target EGF, with cross-correlation of these two close or below 0.5. Tests (e) and (f) are expected to fail at recovering target STFs, as the prior EGF is calculated with a strongly incorrect velocity model. Parameters and full results are in Suppl. Mat. Table S3 and Figs S1 and S2.

sees a time shift (changes in depth, location, velocity structure) or variations of up to  $\sim 20^{\circ}$  in Kagan angle.

Occasionally, our test fails. We consider there is failure when STFs inferred with the DeepGEM-EGF approach do not match the target or overfit noise. These failures usually occur when the prior EGF deviates too much from the target one, for instance with Kagan angles exceeding 20° or when the assumed velocity model significantly differs from the true one (Suppl. Mat. Fig. S1). Good representatives are tests (e) and (f) (Fig. 2 and Suppl. Mat. Fig. S2): for case (e), the STF shape is correct but the length is overestimated, with a very large posterior uncertainty. In test (f), the estimate is a local minimum: inaccuracies in the assumed EGF are mapped in the inferred STF. Such failures can be detected for real cases, as they share specific characteristics: large data residuals, noisy estimated EGFs, large posterior uncertainty on STF or, in contrast, inferred STF with noise (or inaccuracies) overfitting and small posterior uncertainty (Fig. 2 and Suppl. Mat. Figs S1,2). In practice, such mismatch between prior and true forward models are rare due to the careful selection of EGFs.

# 4 Case study: the 2016 Borrego Springs sequence, CA

As first case study, we analyze apparent STFs for an Mw 5.2 event that occurred near Borrego-Springs, CA, USA, in 2016. This earthquake nucleated in the trifurcation area of the San Jacinto Fault Zone, and its rupture propagated unilaterally to the northwest (Ross et al., 2017). We use as EGF a neighbor ML 3.37 event that occurred in 2014. We select this pair of events because of the quality and diversity of available waveforms, and because the apparent STFs that have already been estimated in the time domain show clear directivity (Ross et al., 2017). We select stations within 200 km of this event, and we use high broadband data, bandpassed filtered between 0.1 and 30 Hz and decimated to 50 Hz (see Suppl. Mat. S4). We use P arrivals: our time window starts 1 sec before P arrivals and ends at S arrivals. We use P arrivals for comparison with the results of Ross et al. (2017); S-waves could have been used as well as demonstrated with the Cahuilla case (see section 5).

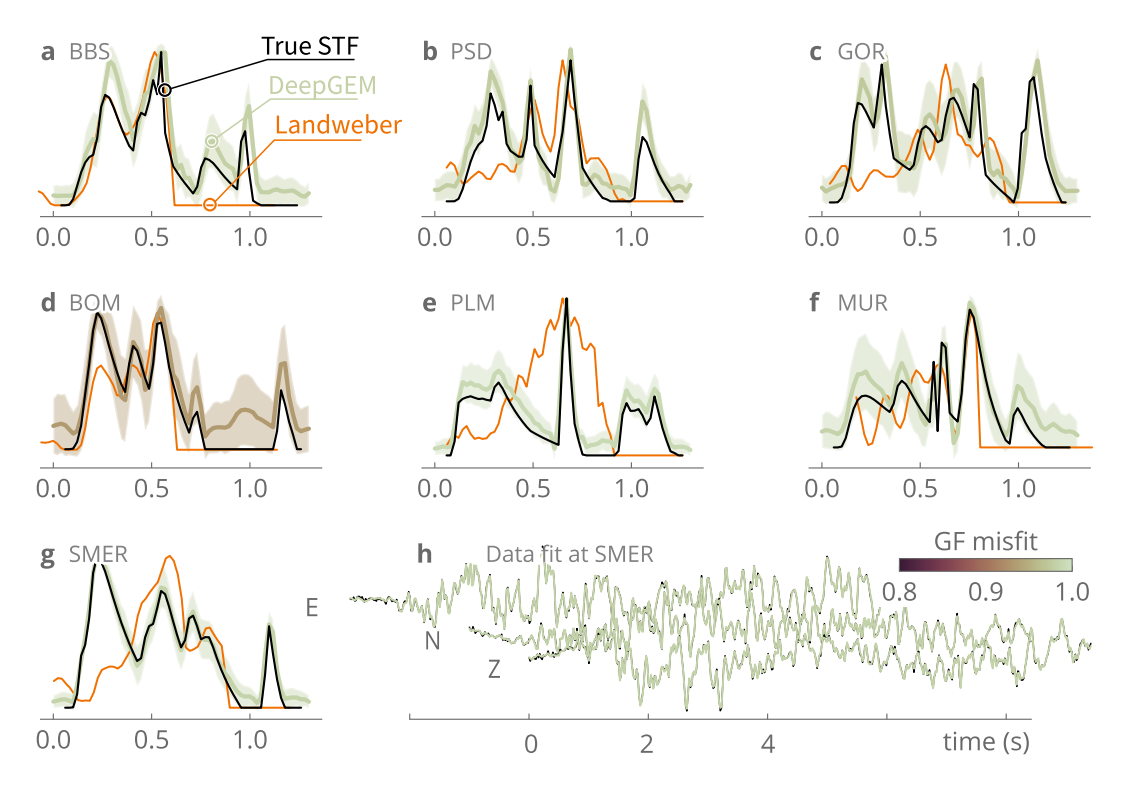


Figure 3. (a) to (g) Inferred (colormap) and target (black) Source-Time Functions (STFs) for synthetic tests designed with waveforms (P arrivals only) recorded for a  $M_L$  3.37 event that occurred in 2014 near Borrego Springs (CA). The mean of the STFs is colored from the cross-correlation between inferred and target Empirical Green's functions; the standard deviation is shaded. Apparent best fitting STFs calculated with the approach of Bertero et al. (1997) are shown in orange. Stations locations are shown in Figure 5. (h) Data fit at station SMER, colored from the misfit between inferred and target EGFs.

#### 4.1 Synthetic tests

To benchmark the approach within a real framework, we first design a few synthetic tests: we convolve synthetic STFs with EGF waveforms and attempt to recover the synthetic STFs. Synthetic STFs are multi-peaked STFs (7 pulses, similarly to the toy models described in section 3, see Suppl. Mat. S4), with have a duration of  $\sim 1\text{-}1.2$  sec, as previously inferred for the Mw 5.2 event (Ross et al., 2017). We add noise to EGF waveforms before convolution, and after. The problem might seem simple, but because of the complexity of the assumed STF and the additional noise, it becomes very ill-posed.

The results of this experiment are consistent with those of the preliminary toy models. We recover all sub-events of the target STFs, and the target is usually within posterior uncertainties (Fig. 3). We note some occasional misfit in amplitude for a few peaks. Target EGFs are well recovered. Data fit is very good (Fig. 3h and Suppl. Mat. Fig. S3). We also infer apparent STFs with the Landweber approach. Baseline STFs are fair to poor, and when fair (stations BBS, BOM) only a subset of the STF sub-events is retrieved. We suppose that the baseline approach performs poorly, in that case, because of the complexity of target STFs and the ill-posedness of the problem.

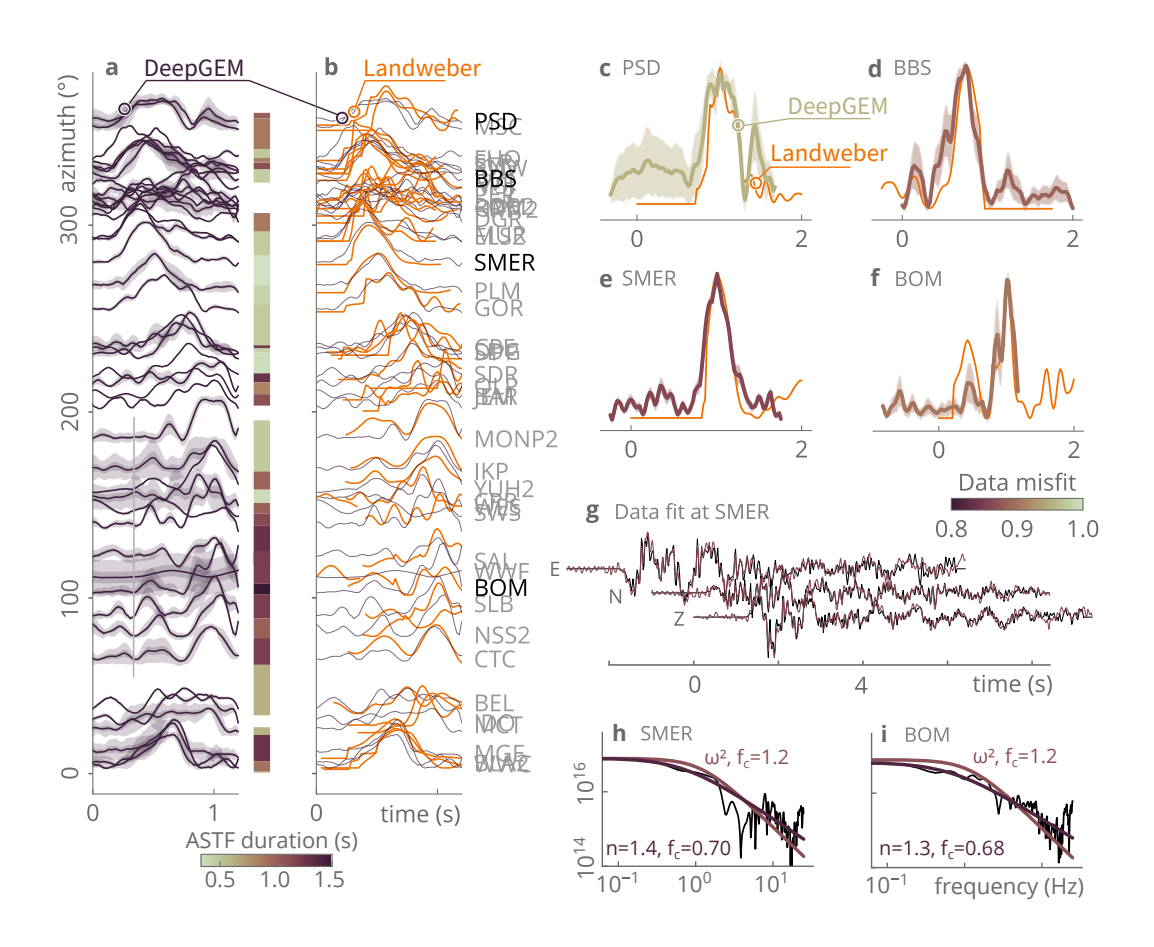


Figure 4. Inferred apparent STFs, data fit, and derived spectra for the 2016 Mw 5.2 main-shock that occurred near Borrego-Springs, CA, USA, using as EGF a neighbor ML 3.37 event that occurred in 2014. (a) STFs inferred with DeepGEM, with a posteriori smoothing; a few stations locations are shown in Figure 5. The duration of each ASTF is plotted on the side. (b) STFs inferred with the approach of Bertero et al. (1997). (c) to (f) Inferred STFs at a few selected stations colored from the misfit (peak cross-correlation) between data and predictions. (e) Data fit at station SMER, colored from the data misfit. (h,i) Normalized moment spectra (N·m) derived from the ASFTs at stations SMER and BOM. The best fitting Brune model and parameters (decay n and corner frequency  $f_c$ ) are shown; an  $\omega^2$  model is also shown for comparison.

4.2 Results

We then estimate apparent STFs for recordings of the Mw 5.2 event at selected stations (Fig. 4). Inferred ASTFs for neighbor stations or stations with similar azimuth share comparable shape; for instance around 360° in azimuth. Moreover, results have a low posterior uncertainty and a good data fit, with a cross-correlation between data and prediction that is usually above 0.8 (Fig. 4g), which altogether suggest inferred STFs are robust. DeepGEM-EGF estimates are close to STFs estimated with the Landweber approach and to the ASTFs of Ross et al. (estimated with a different iterative approach by Kikuchi and Kanamori (1982) and Ligorría and Ammon (1999)).

We estimate ASTFs durations by selecting the signal that exceeds 20% of the peak moment rate (following Courboulex et al., 2016). For a few stations, DeepGEM-EGF results do show more pulses and a longer duration than Landweber estimates (with two clear pulses of up to 1.4 s in duration, especially around 100° in azimuth). Both our and baseline ASTFs (including Ross et al. ones) show a single narrow pulse of ~0.5 sec around 250° (stations SMER). This azimuthal variation can reflect rupture directivity towards the NW, as already suggested by Ross et al. (2017). DeemGEM-EGF-inferred average ASTFs durations (~0.8 s), similar to baseline estimates, are relatively short compared to other events of similar magnitudes. This is comparable to short durations measured for events in the vicinity (see discussion in Ross et al., 2017).

We also derive spectra from the inferred STFs (Figs 4, Suppl. Mat. S4). We pad the ASTFs with zeros for 5 times their length to better constrain the low frequencies, perform a fast Fourier transform and resample the obtained spectra in the logarithmic scale. We then estimate, with simple least-squares in the frequency domain, best fitting Brune source model parameters: decay n and corner frequency  $f_c$  (Brune, 1970). As DeepGEM-EGF results are normalized, we rescale the spectra to  $M_0$  and divide by the average spectra amplitude at all stations. Estimated spectra diverge from classic  $\omega^2$  Brune model, with a decay of 1.47 and a  $f_c$  of 0.6 on average. The deviation is stronger for some stations, and mostly affects the 0.5-5 Hz frequency range. The best-fitting  $\omega^2$  model, with a  $f_c$  of 1.2, would give a Brune stress-drop of 28 GPa. This is comparatively smaller than the static stress drop estimated in the range 49–85 MPa from their finite-fault model by Ross et al. (2017), but remains higher than what is typically observed for similar earthquakes.

The low variability of STFs inferred with different approaches (DeepGEM and baselines) suggests that the prior EGF is probably of good quality. And indeed, inferred EGFs are close to the prior (Suppl. Mat. Fig. S3). In summary of this first test case, when the prior EGF is good, DeepGEM-EGF performs as well as baseline approaches for simple STFs, or better for apparents STFs that contain multiple pulses (or sub-events). Our analysis of the spectra also suggests that common spectral analyses can be applied to ASTFs produced by the proposed approach.

# 5 Case study: the 2016-2019 Cahuilla swarm, CA, USA

The Cahuilla swarm outlined a complex but well-defined fault structure between the San Jacinto and Elsinore fault zones (Fig. 5). Ross et al. (2020) produced a seismicity catalog of more than 22,000 events with Mw ranging from 0.7 to 4.4, all of those event seemingly affecting the same non-planar fault geometry. The main event (Mw 4.4) is ~5 km deep and likely caused drastic changes in the evolution of the swarm by allowing fluids to circulate at shallower depth. We take advantage of this detailed seismic catalog, with many small events, to investigate the impact of forward model assumptions on our knowledge of the source. Along with evaluating the robustness of our approach and the effect of an ad-hoc selection of EGFs on the inference of source parameters, we aim to better characterize the source process of this puzzling event.

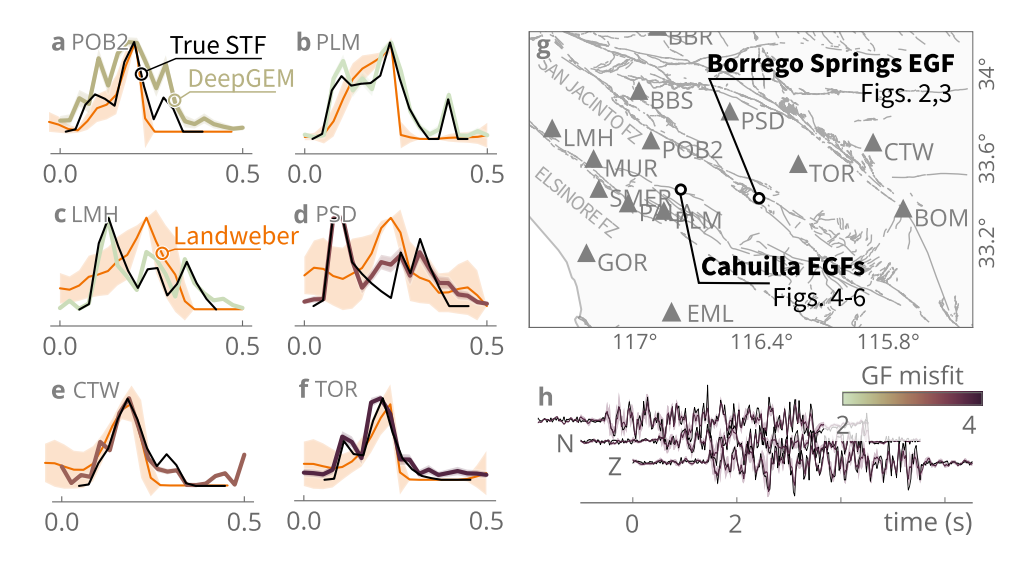


Figure 5. (a-f) Inferred (colored) and target (black) STFs for synthetic tests designed with waveforms (P arrivals) recorded for four neighbor M~2 events that occurred during the Cahuilla swarm. The mean of the STFs is colored from the misfit between inferred and target EGFs; the standard deviation is shaded. (h) Mean inferred (colored) and target (black) EGF at station TOR. (g) Stations locations.

We use broadband seismic data recorded in Southern California for the 2018 Mw 4.41 mainshock and several M~2-2.5 events that occurred during the Cahuilla swarm. We use stations located within 200 km of the mainshock. We use P arrivals or S arrivals, bandpass filtered between 0.1 and 40 Hz and decimated to 40 Hz. For S arrivals, our time window ends 13 sec after S arrivals. We select 1 to 4 prior EGFs, with a 2 <Mw< 2.5, from the cross-correlation of their waveforms with the mainshock waveforms at each station. EGFs are at a distance of less than 1 km from the mainshock, after the relocated catalog from (Ross et al., 2020). The number of assumed EGFs depends on their SNR that should be larger than 2. This amounts to a total of 69 events.

# 5.1 Synthetic tests with multiple EGFs

We first design synthetic tests to benchmark our approach using multiple EGFs as priors, and investigate the impact of the selection of those prior candidates on the results. The target EGF, or the one convolved with synthetic STFs to obtain synthetic mainshock waveforms, is now defined as a random weighted sum of up to 4 prior EGFs. The synthetic STF is multi-peaked (3 pulses), with a duration ranging from 0.2 to 0.5 sec to simulate a M4 event (Suppl. Mat. S5). We use P arrivals.

Using multiple EGFs as priors, we are able to correctly recover all sub-events of target STFs (Fig. 5), with some occasional misfit in amplitude for some peaks. Misfit between data and predictions is low (Suppl. Mat. Fig. S5). In general, the inferred EGF which shows the lower data misfit is the one whose prior was the closest to the target EGF, which is an expected behavior. However, EGFs estimated from an incorrect prior (Suppl. Mat. Fig. S5f for instance) also show a relatively good data fit. Target EGFs are usually well within posterior uncertainties of inferred mean EGFs (Fig. 5h). From our comparisons with results of the Landweber approach, DeepGEM-EGF outperforms two potentially systematic artifacts in baseline approaches: more than three STF sub-events cannot be imaged, and STFs are often inaccurately imaged as highly asymmetric, with an incorrect sharp change in amplitude.

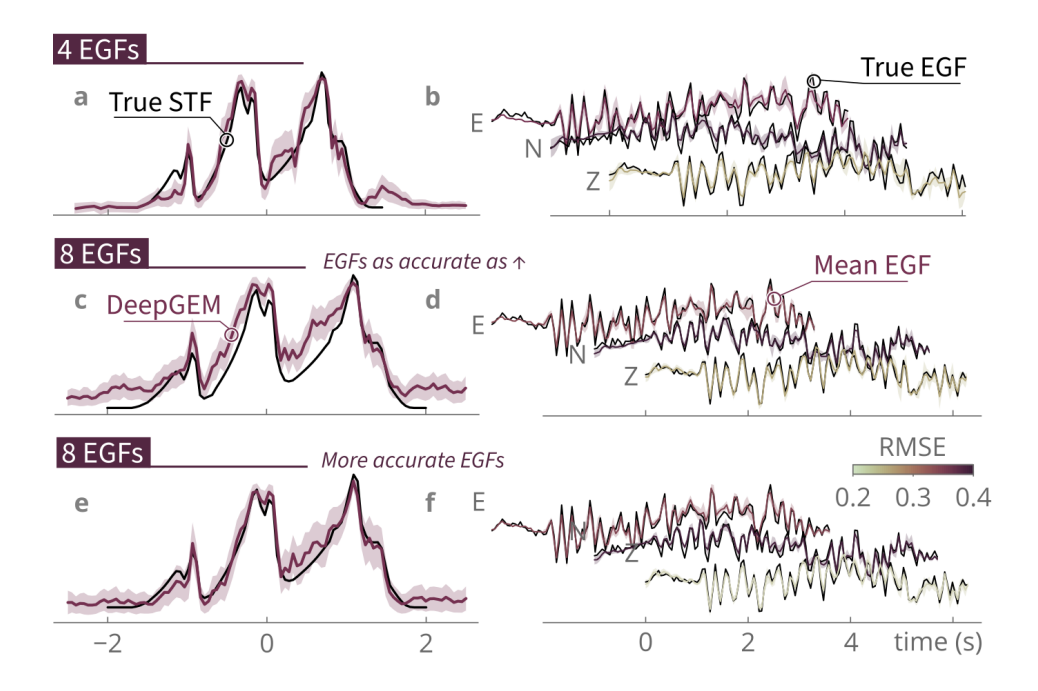


Figure 6. Synthetic tests designed to analyze the impact of added information, using four (a,b) or eight (c-f) prior EGFs, using  $M\sim2$  events that occurred during the Cahuilla swarm. Mean inferred (colored) and target (black) Source-Time Functions (STFs) (left) and Empirical Green's Functions (right) for P arrivals only. In (e,f) the additional four waveforms are closer to the target than in (c,d). Standard deviation ( $1\sigma$ ) is shaded. EGFs are colored by the root mean squared error (RMSE) between data and average predictions normalized for each component.

We perform a few other tests to analyze how adding information, or how increasing the number of prior EGFs, impacts our inference. The idea behind those tests is not to be realistic, but to increase the complexity of the problem by adding parameters to resolve (ie longer STF length). We focus on station TOR, with a target STF of 7 pulses, and with a duration of 4 sec. Waveforms are decimated to 20 Hz. We use 4 prior EGFs in the control test (Fig. 6a,b) and use 4 additional prior EGFs in two other tests. In one case (Fig. 6c,d), the additional four waveforms are random linear combinations of the initial four prior EGFs: in other words, the additional waveforms do not contain more information than the initial four. In the last case, the additional four waveforms are closer to the target EGF: they are equal to the target EGF to which 10% of the random linear combination is added (Fig. 6e,f). As expected, if additional EGFs do not add information content, the inferred model is not improved. In contrast, adding informative EGFs (i.e. more accurate EGFs) improves the quality of the inferred STF. Adding information only very slightly improves the fit to the data. It is therefore more efficient to assume a few

#### 5.2 Results

well selected prior EGFs than multiple poorly constrained priors. These tests further

confirm the robustness of DeepGEM-EGF, and its capacity to use good information.

We first estimate STFs from the set of prior EGFs we selected based on cross-correlation. Then, we analyze the effect of the choice of prior EGFs on our inference. We compare all results to Landweber STFs. DeepGEM-EGF estimates converged well for every station, and data fit is good (Fig. 7, Suppl. Mat. Fig. S6). Apparent STFs duration varies between 0.25 (station EML, Fig. 7g) and 0.6 sec (PSD, Fig. 7f). To the N of the Cahuilla

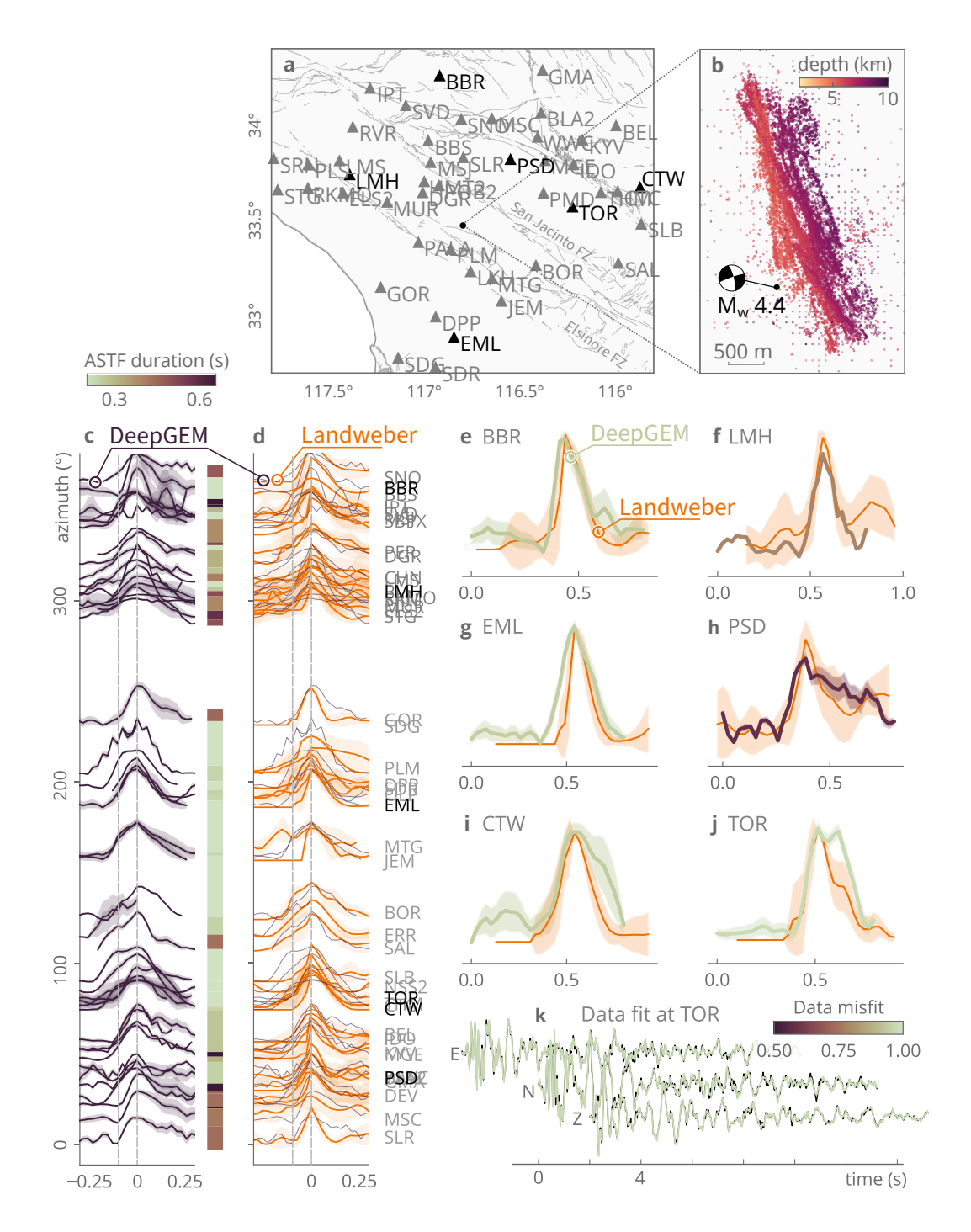


Figure 7. Apparent STFs inferred for the 2018 Mw 4.41 main shock of the Cahuilla swarm, assuming the same prior EGFs as in Fig. 5. (a) Map with stations locations. (b) Relocated catalog for the swarm, from Ross et al. (2020). (c) ASTFs inferred with DeepGEM-EGF with posterior smoothing. The duration of each ASTF is shown on the side. (d) ASTFs estimated with the approach of Bertero et al. (1997). (e-j) Comparison of the results of the two different approaches at a few stations, colored from their data misfit (cross-correlation between data and predictions). Note that  $\sigma$  estimates for the Landweber approach derive from the variability of multiples EGFs and their components, and not from posterior PDFs as for DeepGEM-EGF results. (k) Data fit at station TOR from the DeepGEM-EGF ASTF.

swarm (from about 300 to 45°), apparent STFs are long in duration, with an energetic onset and a long decrease in amplitude (in particular around station PSD). To the South (station EML), apparent STFs are short and more symmetric in shape. The variation in apparent STFs shapes could reflect an along-strike directivity of the Mw 4.4 event towards the southern portion of the fault.

 STFs inferred with the Landweber approach agree with DeepGEM-EGF estimates to a certain degree. For some stations, estimates are similar (stations GOR or BOR for instance, 220 and 120° respectively). For other stations (from 50 to 200° i nazimuth), baseline results often under-estimate STF durations by introducing a delayed sharp increase in amplitude (see station EML for instance): this corresponds to the artifacts observed with our synthetic tests. While STFs at neighbor stations are identical when estimated with DeepGEM-EGF (JEM and MTG at 170°), they can differ strongly when inferred with the Landweber approach, suggesting the baseline approach is less robust.

We also compare apparent STFs inferred assuming various sets of prior EGFs. This time, we decimate waveforms to 20 Hz to decrease computation time. Our preferred results (Fig. 7a, 40 Hz) have been estimated with priors that minimize cross-correlation, using P arrivals (Suppl. Mat. Fig. S7c with 20 Hz). We test 3 other sets of prior EGFs at 20 Hz: (set 1) using S arrivals; (set 2) minimizing distance; (set 3) minimizing cross-correlation at one station (respectively Suppl. Mat. Fig. S7d,a and b). In set (3), selected EGFs are less than 1 km away from the mainshock and maximize the cross-correlation with the mainshock waveforms at station PLM. This choice of station is based on the quality of the waveforms and the deconvolution with set (2). We use identical hyperparameters for all tests. We expect the STFs inferred with set (3) to be the worst estimates, as EGFs are incorrectly constrained with a single station.

For all sets of EGFs, inferred STFs share similar first-order characteristics: width, shape and azimuthal variations (Suppl. Mat. Fig. S7). STFs estimated with set (2) show a good coherence with our preferred results. As expected, STFs estimated with set (3), while consistent between neighbor stations, show many high frequency peaks, which could be noise (or artifacts) overfitting. Small posterior uncertainty on both STFs and EGFs might suggest that over-constraining EGFs to an incorrect prior induced the model to fall into a local minimum.

Increasing the frequency content of the data from 20 to 40 Hz (Fig. 7a with 40 Hz, Suppl. Mat. Fig. S7c with 20 Hz) allows us to refine the imaged complexity of the ASTFs: sub-events are more sharply imaged because there are more data points to exploit. Subevents of shorter duration can also be estimated. Other characteristics (duration, start-end times for instance) are not much impacted. In the other hand, increasing the frequency content rises the potential for noise overfitting (for instance at station DPP, below station PLM in azimuth in Fig. 7a). The choice of the sampling frequency will therefore be dictated by the targeted complexity to image, that trades off with the expected duration of the target ASTF. On the other hand, adding informative EGFs (Fig. 6) could prevent noise overfitting and allow the use of higher frequencies.

As for any inverse problem, we cannot conclude on which STF estimates are the closest to reality. However, because of the similarity of the results for neighbor stations, and the stability of DeepGEM-EGF estimates even for various sets of priors, we can affirm that our results are robust. In complement, the slight variability of our estimates made for various sets of priors suggests that DeepGEM-EGF remains sensitive to the prior selection of EGFs, as expected: the careful selection of a set of good candidate EGFs remains

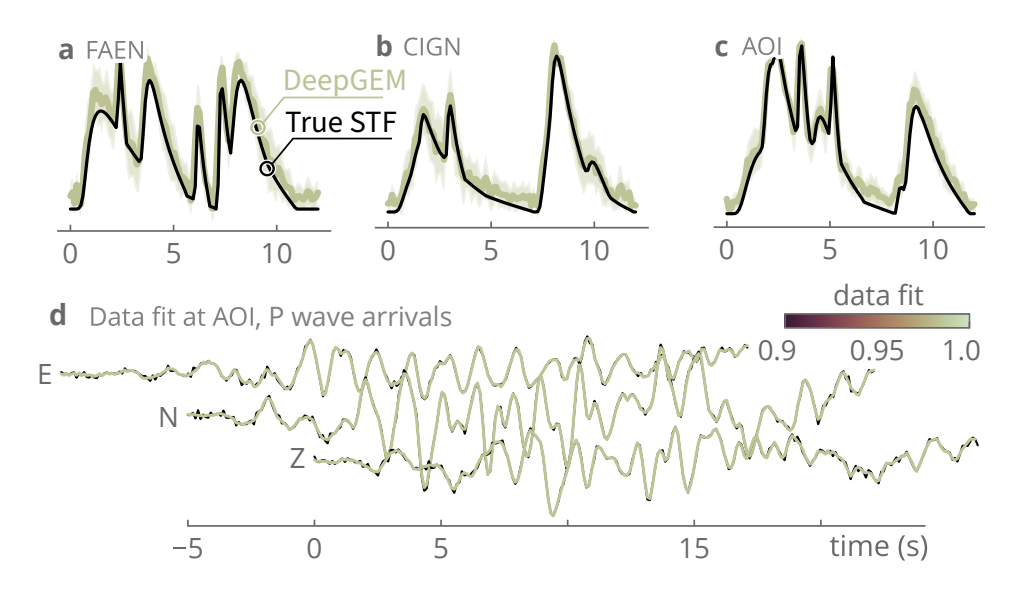


**Figure 8.** (a-c) Inferred (colored) and target (black) STFs for synthetic tests designed with P arrivals recorded for the best EGF selected for the 2009 Mw 6.3 L'Aquila earthquake, Italy. The mean of the STFs is colored from the misfit between inferred and target EGFs; the standard deviation is shaded. (h) Mean inferred (colored) and target (black) EGF at station AOI. Stations locations are in Fig 9.

#### 6 Case study: the 2009 Mw 6.3 l'Aquila earthquake, Italy

465

466

469

470

471

473

474

475

476

477

479

480

481

482

483

485

486

487

Finally, we apply our approach to a larger event: the Mw 6.3 L'Aquila earthquake that occurred in Italy in 2009. This event has been intensively studied. Our goal here is not to deepen our understanding of this event, if even possible, but rather to benchmark our approach with the knowledge that has already been accumulated for this earthquake.

We select stations within 200-500 km of the main shock and use broadband data. Candidate EGFs should be located at less than 3 km from the main shock, have a 3.8<Mw<4.9, a Kagan angle with the main shock of less than 15 and an SNR larger than 1. From those candidates, we select at most 3 EGFs with the best cross-correlation of P arrivals with those of the main shock. We bandpass filter between 0.1 and 2 Hz and decimate the waveforms to 6 Hz. We use either P or S arrivals. For S arrivals, our time windows covers 100 sec.

#### 6.1 Synthetic tests

The design of these tests is similar to the ones previously presented; we use the best EGF (with the highest cross-correlation) and a target STF with 7 peaks and a duration of 12 sec. The fit to target STFs and data is very good (Fig. 8, Suppl. Mat. Fig. S8,S9). For some stations, we slightly overfit the noise: unfiltered noise from the data is mapped on the posterior STFs (see Fig. 8b at 5-6 sec.).

#### 6.2 Results

We estimate apparent STFs at a few stations with both P and S arrivals (Fig. 9). Data fit is fair to good for all stations, with a relatively small posterior uncertainty (Suppl. Mat. Fig. S10,S11 at station AOI). We note a clear divergence in the shape of apparent STFs depending on their azimuth. To the north, inferred ASTFs show two main sub-events, one

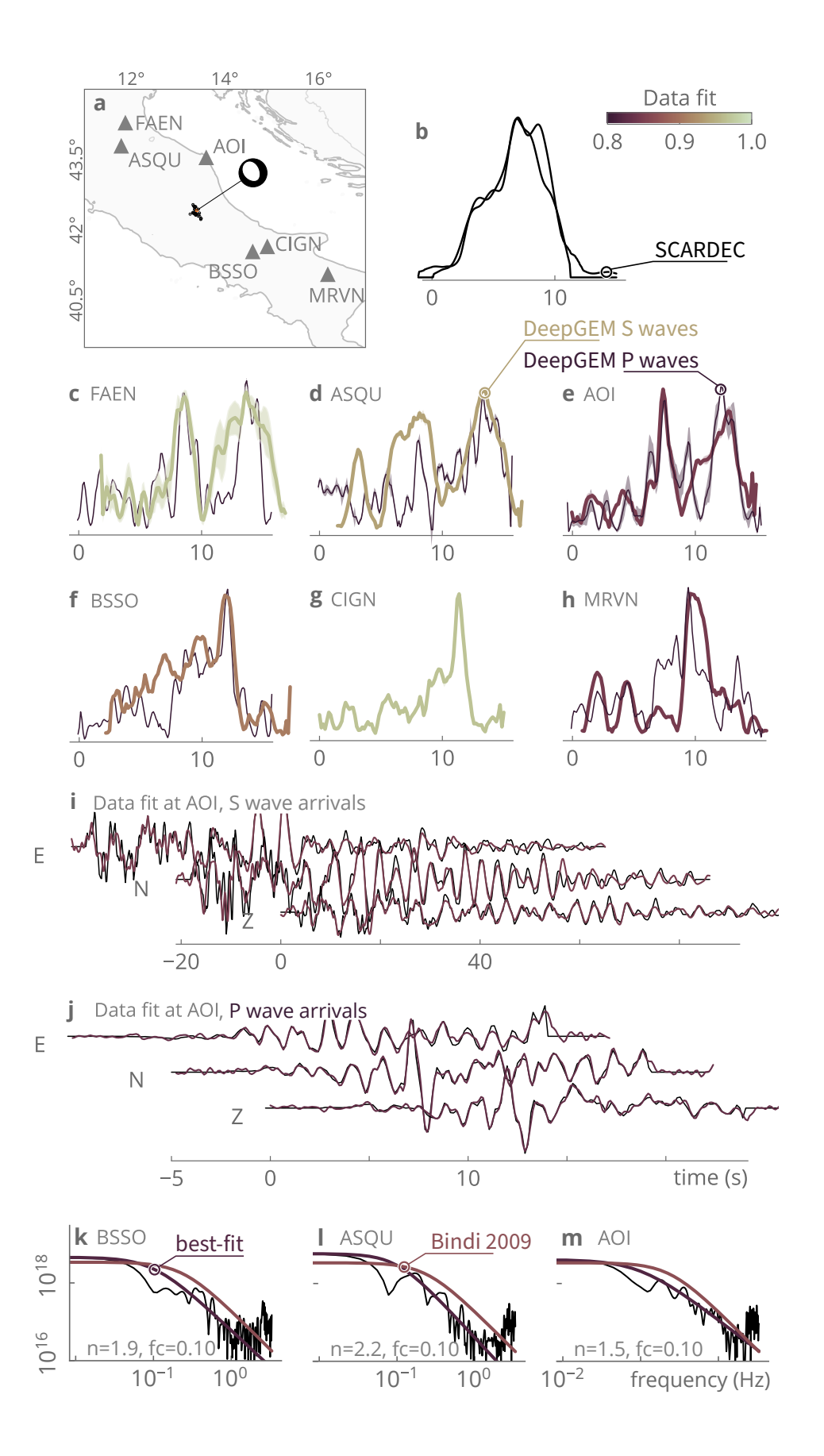


Figure 9. Apparent STFs, data fit, and derived spectra, inferred for the 2009 Mw 6.3 L'Aquila earthquake, Italy. (a) Map of the selected stations locations and EGFs used (black dots). (b) SCARDEC solutions for the apparent STFs (Vallée et al., 2011). (c-h) Apparent STFs estimated with DeepGEM-EGF using S arrivals (colored from data misfit) or P arrivals (deep purple). (i) Data fit at station AOI for DeepGEM-EGF estimates with S waves arrivals. (j) Data fit at station AOI for DeepGEM-EGF estimates with P waves arrivals. (k-m) Rescaled S-waves moment spectra (N·m) for selected stations, fitted with a Brune source model of varying decay n. The Brune model estimated by Bindi et al. (2009) is shown for comparison.

with a duration of 2-4 sec, and the later one with a duration of 5-6 sec. The duration of the first peak is shorter when P waves are used. The total duration of those ASTFs is of ~10 sec. In contrast, to the south, S-waves ASTFs are characterized by a single longer peak, from 6 sec (station MRVN) to 12 sec in duration (station BSSO), with an amplitude that increases gradually. With P waves, we rather observe a 6-8-sec-long main peak, preceded by a 7 sec sub-event of small amplitude.

The duration of inferred ASTFs agrees well with the 10-11 sec duration that has been estimated with teleseismic data (for both finite-fault studies: Poiata et al. (2012); Yano et al. (2014); Balestra and Delouis (2015); and SCARDEC estimates: Vallée et al. (2011); Vallée and Douet (2016)). The shape is also coherent with what has already been published, with an asymmetric shape characterized by a slow increase followed by a sharper drop in amplitude. The difference in duration for ASTFs observed at different azimuth agrees with the observed directivity of the mainshock towards the SE (e.g. Cirella et al., 2012; Yano et al., 2014; Avallone et al., 2011). Orefice et al. (2013) estimated ASTFs at several broadband stations using surface waves and one Mw 4.9 aftershock as EGF. Although we did not analyze similar stations or data, our results well correspond. They observed long ASTFs with two main peaks, clearly separated, north of the rupture; and a single short main peak with either two or one subevent to the south-east and south.

We also derive spectra from our S and P-waves ASTF estimates following the approach described in section 4.2. Obtained spectra do show a clear deviation from an  $\omega^2$  Brune model (see the model of Bindi et al. (2009) for reference in Fig. 9 and Suppl. Mat. Fig. S12,S13), especially at frequencies around 0.1 Hz. Inferred decay is of 1.7 and corner frequency of 0.1 on average at all stations (with frequencies > 1.25 Hz discarded from the fit). The frequency corner inferred by Bindi et al. (2009) from S wave spectra is always too large to fit our spectra. As a consequence of this deviation from the omega-squared model, derived Brune stress-drop values ( $\Delta \sigma = 0.71$  MPa, using  $\beta = 3.5$ km/s) are smaller than the stress drop of ~9 MPa that has been inferred with  $\omega^2$  models (e.g., Bindi et al., 2009, using the same assumptions) or finite-fault studies (e.g., Poiata et al., 2012; Gaudio et al., 2015; Ameri et al., 2011; Calderoni et al., 2013). The deviation from the  $\omega^2$  model is even stronger for P waves (see P waves spectra in Suppl. Mat. Fig. S13). There also is a clear increase of high frequency content (>1Hz), in particular for S waves. From our synthetic tests, this increase in HF content is potentially related to noise overfitting, but remains to be investigated.

#### 7 Discussion and conclusions

We introduce DeepGEM-EGF, a Bayesian joint inversion method for the source deconvolution problem. DeepGEM-EGF explicitly accounts for epistemic uncertainties and provides probabilistic estimates of apparent source time functions in the time domain, advancing beyond deterministic methods. DeepGEM-EGF can use multiple EGFs as priors, and derive posterior uncertainties for EGFs. We show through tests on simple toy models, synthetic tests and several case study, that this approach effectively discriminates source parameters given approximations made in the forward model.

We analyzed a broad range of frequency—magnitude data, with main events from Mw 4.4 to Mw 6.3. Our benchmarks demonstrate that DeepGEM-EGF delivers more robust and coherent results than baseline methods. In particular, the proposed approach provides improved estimates of high-frequency content, and the resulting ASTFs are free from systematic artifacts (e.g., those affecting shape or duration in baseline methods). Although DeepGEM-EGF remains stable for various choices of prior EGFs, we show that the selection of good EGFs conditions the quality of the results. Indeed, incorrect priors might bias the inference towards local minima. Our findings also suggest that a few well-chosen, informative priors outperform numerous weakly constrained ones.

The proposed approach may underperform. Highly underdetermined scenarios, for which the time window of considered data is too short for the duration of the STF, can be problematic. When prior EGFs deviate significantly from the true solution, i.e. when the EGF assumption does not hold anymore, DeepGEM-EGF can fail to converge. In our tests, such scenario occurred only for cases where the EGF assumption was deliberately relaxed: diverging focal mechanism, different velocity model, high and unfiltered noise,

In practice, the reliability and robustness of DeepGEM-EGF results can be analyzed from a variety of factors. Successful synthetic tests, and the similarity of imaged ASTFs for neighbor stations, can guarantee qualitative results. In contrast, overfitted STFs (noisy, with many peaks) combined with a small posterior uncertainty; or abnormally large posterior uncertainty; often reflect a poor resolution of the problem. Data fit and the similarity of posterior and prior EGFs are user-tuned hyperparameters that need to be interpreted with caution. When using several priors, an intuitive interpretation could be that robust estimates necessarily induce high correlations among posterior EGFs. This is only true when the assumed set of priors EGFs is well chosen and already coherent. However, posterior EGFs can also be coherently inaccurate when priors are incorrect, which leads the model to be trapped in a local minimum.

Relatively to baseline methods, DeepGEM-EGF improvements are modest for simple STFs if the EGF is well selected. Performance significantly improves for complex, multi-peaked source functions and/or if the EGF candidates are poor choices. Previous comparison studies have already shown that agreement between methods degrades as source complexity increases (e.g., Abercrombie, Chen, et al., 2025), reflecting the growing ill-posedness of the inverse problem. In such cases, DeepGEM-EGF closely matches synthetic targets. With real data, inferred STFs are more complex than baseline estimates, with more sub-events imaged. Estimated spectra usually diverge from the omega squared model. Whether this added complexity reflects true source behavior remains to be further investigated, though synthetic tests support its plausibility.

Understanding earthquake self-similarity across scales is crucial for advancing physical models and improving hazard assessments. Self-similarity is often explored using two key proxies: source complexity and stress drop. Both stress drop (Atkinson & Beresnev, 1997; Abercrombie, 2021; Bindi et al., 2023; A. Baltay et al., 2024; Neely et al., 2024) and metrics of source complexity (Vallée & Douet, 2016; Danré et al., 2019; Pennington et al., 2023; Neely et al., 2024) are uncertain and variable. Yet, such proxies are increasingly more difficult to constrain for events of decreasing magnitude, because of both data and methodological limitations. On one hand, shorter rupture durations concentrate energy at higher frequencies: limited bandwidth, reduced signal-to-noise ratio (in particular in the HF), and sparse azimuthal coverage, will degrade the available information about source complexity, probably down to an instrumental limit (e.g., Abercrombie, 2015). On the other hand, any epistemic uncertainty introduced in the problem will have a stronger impact on estimated parameters (e.g., A. Baltay et al., 2024; Abercrombie, Baltay, et al., 2025).

Discriminating variability in source properties from artifacts induced by epistemic uncertainties is therefore even more difficult for, but maybe even more important for our understanding of, events of decreasing magnitude. We show with synthetic tests that DeepGEM-EGF is able to recover complex ASTFs for magnitudes ranging from 4 to 6.3. With real data, we image relatively simpler source functions for the Mw 4 event, and robust features (e.g., shared by neighbor stations) only include one main pulse. By contrast, we image complex STFs (with multiple sub-events) for the events with Mw>5. Our results, whilst limited to 3 test cases, therefore seem to suggest that the level of complexity of the source, when using the number of sub-events as metric, increases as a function of magnitude (e.g., Danré et al., 2019). Because of potential data limitations, we

chose here to focus our benchmark on minor to large earthquakes; the robustness and relevance of our approach will have to be tested for smaller events.

With this paper, we have shown that DeepGEM-EGF has the potential to help answer challenges related to questions of self-similarity, by reliably imaging complex, multi-peaked STFs under noisy conditions, while staying methodologically consistent across minor to large magnitudes (e.g., Neely et al., 2024; A. Baltay et al., 2024). We aim for this joint approach to become a valuable tool for disentangling the variability of the seismic source, and potentially stress drop, from artifacts introduced by modeling assumptions. DeepGEM-EGF is available as an open-source tool.

### Open Research

DeepGEM-EGF is available at Ragon (2024). A running example is available on the same repository. We used waveform data provided by the regional (CI, California Institute of Technology and United States Geological Survey Pasadena, 1926), ANZA (AZ, Vernon, 1982) and UCSB (SB, UC Santa Barbara, 1989) networks in Southern California, and the Italian National Seismic Network (IV, Istituto Nazionale di Geofisica e Vulcanologia (INGV), 2005). Our approach expands on DeepGEM (A. F. Gao et al., 2021), which is available at A. Gao (2021).

### Acknowledgements

We thank Mathieu Causse and Emile Denise for fruitful discussions. We thank the editor, Rachel Abercrombie, and Daniel Trugman along with two anonymous reviewers for their suggestions that greatly helped to improve the manuscript. ZR is supported by the David and Lucile Packard Foundation and the US National Science Foundation.

References

- Abercrombie, R. E. (2015). Investigating uncertainties in empirical Green's function analysis of earthquake source parameters. *Journal of Geophysical Research:* Solid Earth, 120(6), 4263–4277. doi: 10.1002/2015JB011984
- Abercrombie, R. E. (2021). Resolution and uncertainties in estimates of earthquake stress drop and energy release. *Philosophical Transactions of the Royal Society A: Mathematical, Physical and Engineering Sciences*, 379(2196), 20200131. doi: 10.1098/rsta.2020.0131
- Abercrombie, R. E., Baltay, A., Chu, S., Taira, T., Bindi, D., Boyd, O. S., ... Zhang, J. (2025). Overview of the SCEC/USGS Community Stress Drop Validation Study Using the 2019 Ridgecrest Earthquake Sequence. Bulletin of the Seismological Society of America, 115(3), 734–759. doi: 10.1785/0120240158
- Abercrombie, R. E., Chen, X., Huang, Y., & Chu, S. (2025). Comparison of EGF Methods for Ridgecrest Sequence: Can EGFs Help Resolve Ambiguity in Isolating Source Spectra? Bulletin of the Seismological Society of America, 115(3), 1132–1148. doi: 10.1785/0120240161
- Abercrombie, R. E., Poli, P., & Bannister, S. (2017). Earthquake Directivity, Orientation, and Stress Drop Within the Subducting Plate at the Hikurangi Margin, New Zealand. *Journal of Geophysical Research: Solid Earth*, 122(12), 10,176–10,188. doi: 10.1002/2017JB014935
- Abercrombie, R. E., & Rice, J. R. (2005). Can observations of earthquake scaling constrain slip weakening? Geophysical Journal International, 162(2), 406–424. doi: 10.1111/j.1365-246X.2005.02579.x
- Aki, K. (1967). Scaling law of seismic spectrum. *Journal of Geophysical Research* (1896-1977), 72(4), 1217–1231. doi: 10.1029/JZ072i004p01217

Aki, K. (1996). Scale dependence in earthquake phenomena and its relevance to earthquake prediction. *Proceedings of the National Academy of Sciences*, 93(9), 3740–3747. doi: 10.1073/pnas.93.9.3740

- Ameri, G., Oth, A., Pilz, M., Bindi, D., Parolai, S., Luzi, L., ... Cultrera, G. (2011). Separation of source and site effects by generalized inversion technique using the aftershock recordings of the 2009 L'Aquila earthquake. Bulletin of Earthquake Engineering, 9(3), 717–739. doi: 10.1007/s10518-011-9248-4
- Anderson, J. G., & Brune, J. N. (1999). Probabilistic Seismic Hazard Analysis without the Ergodic Assumption. Seismological Research Letters, 70(1), 19–28. doi: 10.1785/gssrl.70.1.19
- Andrews, D. J. (1986). Objective Determination of Source Parameters and Similarity of Earthquakes of Different Size. In *Earthquake Source Mechanics* (pp. 259–267). American Geophysical Union (AGU). doi: 10.1029/GM037p0259
- Atkinson, G. M., & Beresnev, I. (1997). Don't Call it Stress Drop. Seismological Research Letters, 68(1), 3–4. doi: 10.1785/gssrl.68.1.3
- Avallone, A., Marzario, M., Cirella, A., Piatanesi, A., Rovelli, A., Di Alessandro, C., ... Mattone, M. (2011). Very high rate (10 Hz) GPS seismology for moderate-magnitude earthquakes: The case of the Mw 6.3 L'Aquila (central Italy) event. *Journal of Geophysical Research: Solid Earth*, 116(B2). doi: 10.1029/2010JB007834
- Backus, G., & Mulcahy, M. (1976). Moment Tensors and other Phenomenological Descriptions of Seismic Sources—I. Continuous Displacements. *Geophysical Journal International*, 46(2), 341–361. doi: 10.1111/j.1365-246X.1976.tb04162.x
- Backus, G. E. (1977). Interpreting the seismic glut moments of total degree two or less. *Geophysical Journal International*, 51(1), 1–25. doi: 10.1111/j.1365-246X .1977.tb04187.x
- Balestra, J., & Delouis, B. (2015). Reassessing the Rupture Process of the 2009 L'Aquila Earthquake (Mw 6.3) on the Paganica Fault and Investigating the Possibility of Coseismic Motion on Secondary Faults. Bulletin of the Seismological Society of America, 105(3), 1517–1539. doi: 10.1785/0120140239
- Baltay, A., Abercrombie, R., Chu, S., & Taira, T. (2024). The SCEC/USGS Community Stress Drop Validation Study Using the 2019 Ridgecrest Earthquake Sequence. Seismica, 3(1). doi: 10.26443/seismica.v3i1.1009
- Baltay, A. S., Hanks, T. C., & Beroza, G. C. (2013). Stable Stress-Drop Measurements and their Variability: Implications for Ground-Motion Prediction. *Bulletin of the Seismological Society of America*, 103(1), 211–222. doi: 10.1785/0120120161
- Bell-Kligler, S., Shocher, A., & Irani, M. (2019). Blind Super-Resolution Kernel Estimation using an Internal-GAN. arXiv e-prints, arXiv:1909.06581. doi: 10.48550/arXiv.1909.06581
- Bertero, M., Bindi, D., Boccacci, P., Cattaneo, M., Eva, C., & Lanza, V. (1997). Application of the projected Landweber method to the estimation of the source time function in seismology. *Inverse Problems*, 13(2), 465. doi: 10.1088/0266-5611/13/2/017
- Bindi, D., Pacor, F., Luzi, L., Massa, M., & Ameri, G. (2009). The Mw 6.3, 2009 L'Aquila earthquake: source, path and site effects from spectral analysis of strong motion data. Geophysical Journal International, 179(3), 1573–1579. doi: 10.1111/j.1365-246X.2009.04392.x
- Bindi, D., Spallarossa, D., Picozzi, M., Oth, A., Morasca, P., & Mayeda, K. (2023). The Community Stress-Drop Validation Study—Part I: Source, Propagation, and Site Decomposition of Fourier Spectra. Seismological Research Letters, 94(4), 1980–1991. doi: 10.1785/0220230019
- Boatwright, J. (1984). The effect of rupture complexity on estimates of source size. *Journal of Geophysical Research: Solid Earth*, 89(B2), 1132–1146. doi:

10.1029/JB089iB02p01132

- Boore, D. M. (2003). Simulation of Ground Motion Using the Stochastic Method. In Y. Ben-Zion (Ed.), Seismic Motion, Lithospheric Structures, Earthquake and Volcanic Sources: The Keiiti Aki Volume (pp. 635–676). Basel: Birkhäuser. doi: 10.1007/978-3-0348-8010-7 10
- Brune, J. N. (1970). Tectonic stress and the spectra of seismic shear waves from earthquakes. *Journal of Geophysical Research* (1896-1977), 75(26), 4997–5009. doi: 10.1029/JB075i026p04997
- Calderoni, G., Rovelli, A., & Singh, S. K. (2013). Stress drop and source scaling of the 2009 April L'Aquila earthquakes. Geophysical Journal International, 192(1), 260–274. doi: 10.1093/gji/ggs011
- California Institute of Technology and United States Geological Survey Pasadena. (1926). Southern California Seismic Network. International Federation of Digital Seismograph Networks. doi: 10.7914/SN/CI
- Chu, S., Baltay, A., & Abercrombie, R. (2024). Characterizing Directivity in Small (M 2.4–5) Aftershocks of the Ridgecrest Sequence. Bulletin of the Seismological Society of America, 115(3), 1177–1188. doi: 10.1785/0120240146
- Cirella, A., Piatanesi, A., Tinti, E., Chini, M., & Cocco, M. (2012). Complexity of the rupture process during the 2009 L'Aquila, Italy, earthquake. *Geophysical Journal International*, 190(1), 607–621. doi: 10.1111/j.1365-246X.2012.05505.x
- Cocco, M., Tinti, E., & Cirella, A. (2016). On the scale dependence of earthquake stress drop. Journal of Seismology, 20(4), 1151-1170. doi: 10.1007/s10950-016-9594-4
- Cotton, F., Archuleta, R., & Causse, M. (2013). What is Sigma of the Stress Drop? Seismological Research Letters, 84(1), 42–48. doi: 10.1785/0220120087
- Courboulex, F., Vallée, M., Causse, M., & Chounet, A. (2016). Stress-Drop Variability of Shallow Earthquakes Extracted from a Global Database of Source Time Functions. Seismological Research Letters, 87(4), 912–918. doi: 10.1785/0220150283
- Courboulex, F., Virieux, J., Deschamps, A., Gibert, D., & Zollo, A. (1996). Source investigation of a small event using empirical Green's functions and simulated annealing. *Geophysical Journal International*, 125(3), 768–780. doi: 10.1111/j.1365-246X.1996.tb06022.x
- Danré, P., Yin, J., Lipovsky, B. P., & Denolle, M. A. (2019). Earthquakes Within Earthquakes: Patterns in Rupture Complexity. Geophysical Research Letters, 46(13), 7352–7360. doi: 10.1029/2019GL083093
- Dinh, L., Sohl-Dickstein, J., & Bengio, S. (2016). Density estimation using Real NVP. arXiv e-prints, arXiv:1605.08803. doi: 10.48550/arXiv.1605.08803
- Dreger, D. S. (1994). Empirical Green's function study of the January 17, 1994 Northridge, California earthquake. Geophysical Research Letters, 21(24), 2633–2636. doi: 10.1029/94GL02661
- Fan, W., & McGuire, J. J. (2018). Investigating microearthquake finite source attributes with IRIS Community Wavefield Demonstration Experiment in Oklahoma. *Geophysical Journal International*, 214(2), 1072–1087. doi: 10.1093/gji/ggy203
- Frankel, A., Fletcher, J., Vernon, F., Haar, L., Berger, J., Hanks, T., & Brune, J. (1986). Rupture characteristics and tomographic source imaging of ML  $\sim 3$  earthquakes near Anza, southern California. *Journal of Geophysical Research:* Solid Earth, 91(B12), 12633–12650. doi: 10.1029/JB091iB12p12633
- Frankel, A., & Kanamori, H. (1983). Determination of rupture duration and stress drop for earthquakes in southern California. *Bulletin of the Seismological Society of America*, 73(6A), 1527–1551. doi: 10.1785/BSSA07306A1527
- Gallegos, A., & Xie, J. (2020). A multichannel deconvolution method to retrieve source—time functions: application to the regional Lg wave. *Geophysical Jour-*

nal International, 223(1), 323–347. doi: 10.1093/gji/ggaa303

- Gao, A. (2021). Deepgem [software]. Retrieved from https://github.com/angelafgao/DeepGEM
- Gao, A. F., Castellanos, J. C., Yue, Y., Ross, Z. E., & Bouman, K. (2021). Deep-GEM: Generalized Expectation-Maximization for Blind Inversion. In *Thirty-Fifth Conference on Neural Information Processing Systems*.
- Garcia-Aristizabal, A., Caciagli, M., & Selva, J. (2016). Considering uncertainties in the determination of earthquake source parameters from seismic spectra. *Geophysical Journal International*, 207(2), 691–701. doi: 10.1093/gji/ggw303
- Gaudio, S. D., Causse, M., & Festa, G. (2015). Broad-band strong motion simulations coupling k-square kinematic source models with empirical Green's functions: the 2009 L'Aquila earthquake. Geophysical Journal International, 203(1), 720–736. doi: 10.1093/gji/ggv325
- Gerstenberger, M. C., Marzocchi, W., Allen, T., Pagani, M., Adams, J., Danciu, L., ... Petersen, M. D. (2020). Probabilistic Seismic Hazard Analysis at Regional and National Scales: State of the Art and Future Challenges. Reviews of Geophysics, 58(2), e2019RG000653. doi: 10.1029/2019RG000653
- Godano, M., Bernard, P., & Dublanchet, P. (2015). Bayesian inversion of seismic spectral ratio for source scaling: Application to a persistent multiplet in the western Corinth rift. *Journal of Geophysical Research: Solid Earth*, 120(11), 7683–7712. doi: 10.1002/2015JB012217
- Hardebeck, J. L. (2020). Are the Stress Drops of Small Earthquakes Good Predictors of the Stress Drops of Moderate-to-Large Earthquakes? *Journal of Geophysical Research: Solid Earth*, 125(3), e2019JB018831. doi: 10.1029/2019JB018831
- Hartzell, S. H. (1978). Earthquake aftershocks as Green's functions. *Geophysical Research Letters*, 5(1), 1–4. doi: 10.1029/GL005i001p00001
- Hough, S. E. (1997). Empirical Green's function analysis: Taking the next step. Journal of Geophysical Research: Solid Earth, 102(B3), 5369–5384. doi: 10.1029/96JB03488
- Hutchings, L., & Wu, F. (1990). Empirical Green's Functions from small earthquakes: A waveform study of locally recorded aftershocks of the 1971 San Fernando Earthquake. *Journal of Geophysical Research: Solid Earth*, 95(B2), 1187–1214. doi: 10.1029/JB095iB02p01187
- Ihmlé, P. F. (1996). Monte Carlo slip inversion in the frequency domain Application to the 1992 Nicaragua Slow Earthquake. Geophysical Research Letters, 23(9), 913–916. doi: 10.1029/96GL00872
- Istituto Nazionale di Geofisica e Vulcanologia (INGV). (2005). Rete Sismica Nazionale (RSN). Istituto Nazionale di Geofisica e Vulcanologia (INGV). doi: 10.13127/SD/X0FXNH7QFY
- Kagan, Y. Y. (1991). 3-D rotation of double-couple earthquake sources. Geophysical Journal International, 106(3), 709-716. doi: 10.1111/j.1365-246X.1991.tb06343.x
- Kanamori, H., & Brodsky, E. E. (2004). The physics of earthquakes. *Reports on Progress in Physics*, 67(8), 1429. doi: 10.1088/0034-4885/67/8/R03
- Kane, D. L., Kilb, D. L., & Vernon, F. L. (2013). Selecting Empirical Green's Functions in Regions of Fault Complexity: A Study of Data from the San Jacinto Fault Zone, Southern California. Bulletin of the Seismological Society of America, 103(2A), 641–650. doi: 10.1785/0120120189
- Kane, D. L., Prieto, G. A., Vernon, F. L., & Shearer, P. M. (2011). Quantifying Seismic Source Parameter Uncertainties. Bulletin of the Seismological Society of America, 101(2), 535–543. doi: 10.1785/0120100166
- Kaneko, Y., & Shearer, P. M. (2015). Variability of seismic source spectra, estimated stress drop, and radiated energy, derived from cohesive-zone models of symmetrical and asymmetrical circular and elliptical ruptures. *Journal of Geophys*-

ical Research: Solid Earth, 120(2), 1053–1079. doi: 10.1002/2014JB011642

- Kikuchi, M., & Kanamori, H. (1982). Inversion of complex body waves. Bulletin of the Seismological Society of America, 72(2), 491–506. doi: 10.1785/BSSA0720020491
- Kingma, D. P., & Ba, J. (2014). Adam: A Method for Stochastic Optimization. In 3rd International Conference for Learning Representations. San Diego.
- Lambert, V., Lapusta, N., & Faulkner, D. (2021). Scale Dependence of Earthquake Rupture Prestress in Models With Enhanced Weakening: Implications for Event Statistics and Inferences of Fault Stress. *Journal of Geophysical Research: Solid Earth*, 126(10), e2021JB021886. doi: 10.1029/2021JB021886
- Ligorría, J. P., & Ammon, C. J. (1999). Iterative deconvolution and receiverfunction estimation. *Bulletin of the Seismological Society of America*, 89(5), 1395–1400. doi: 10.1785/BSSA0890051395
- Lin, Y.-Y., & Lapusta, N. (2018). Microseismicity Simulated on Asperity-Like Fault Patches: On Scaling of Seismic Moment With Duration and Seismological Estimates of Stress Drops. *Geophysical Research Letters*, 45(16), 8145–8155. doi: 10.1029/2018GL078650
- McGuire, J. J. (2004). Estimating Finite Source Properties of Small Earthquake Ruptures. Bulletin of the Seismological Society of America, 94(2), 377–393. doi: 10.1785/0120030091
- McGuire, J. J., & Kaneko, Y. (2018). Directly estimating earthquake rupture area using second moments to reduce the uncertainty in stress drop. Geophysical Journal International, 214(3), 2224–2235. doi: 10.1093/gji/ggy201
- McGuire, J. J., Zhao, L., & Jordan, T. H. (2001). Teleseismic inversion for the second degree moments of earthquake space—time distributions. *Geophysical Journal International*, 145(3), 661–678. doi: 10.1046/j.1365-246x.2001.01414.x
- Mueller, C. S. (1985). Source pulse enhancement by deconvolution of an empirical Green's function. Geophysical Research Letters, 12(1), 33–36. doi: 10.1029/GL012i001p00033
- Neely, J. S., Huang, Y., & Fan, W. (2019). Earthquake rupture characteristics along a developing transform boundary. *Geophysical Journal International*, 219(2), 1237–1252. doi: 10.1093/gji/ggz357
- Neely, J. S., Park, S., & Baltay, A. (2024). The Impact of Source Time Function Complexity on Stress-Drop Estimates. Bulletin of the Seismological Society of America. doi: 10.1785/0120240022
- Orefice, A., Vallée, M., Balestra, J., Delouis, B., & Zollo, A. (2013). Refined Rupture-Velocity Estimation of the 2009 L'Aquila Earthquake (Mw 6.3, Central Italy) Derived from Apparent Source Time Functions. Bulletin of the Seismological Society of America, 103(4), 2474–2481. doi: 10.1785/0120120255
- Oth, A., Miyake, H., & Bindi, D. (2017). On the relation of earthquake stress drop and ground motion variability. *Journal of Geophysical Research: Solid Earth*, 122(7), 5474–5492. doi: 10.1002/2017JB014026
- Pavic, R., Koller, M. G., Bard, P.-Y., & Lacave-Lachet, C. (2000). Ground motion prediction with the empirical Green's function technique: an assessment of uncertainties and confidence level. *Journal of Seismology*, 4(1), 59–77. doi: 10.1023/A:1009826529269
- Pennington, C. N., Wu, Q., Chen, X., & Abercrombie, R. E. (2023). Quantifying rupture characteristics of microearthquakes in the Parkfield Area using a high-resolution borehole network. *Geophysical Journal International*, 233(3), 1772–1785. doi: 10.1093/gji/ggad023
- Percival, D. B., & Walden, A. T. (1993). Spectral Analysis for Physical Applications. Spectral Analysis for Physical Applications.
- Plourde, A. P., & Bostock, M. G. (2017). Multichannel Deconvolution for Earth-quake Apparent Source Time Functions. Bulletin of the Seismological Society of America, 107(4), 1904–1913. doi: 10.1785/0120170015

Poiata, N., Koketsu, K., Vuan, A., & Miyake, H. (2012). Low-frequency and broad-band source models for the 2009 L'Aquila, Italy, earthquake. *Geophysical Journal International*, 191(1), 224–242. doi: 10.1111/j.1365-246X.2012.05602.x

- Prieto, G. A., Parker, R. L., Vernon, F. L., Shearer, P. M., & Thomson, D. J. (2006). Uncertainties in Earthquake Source Spectrum Estimation Using Empirical Green Functions. In Earthquakes: Radiated Energy and the Physics of Faulting (pp. 69–74). American Geophysical Union (AGU). doi: 10.1029/170GM08
  - Prieto, G. A., Parker, R. L., & Vernon III, F. L. (2009). A Fortran 90 library for multitaper spectrum analysis. Computers & Geosciences, 35(8), 1701–1710. doi: 10.1016/j.cageo.2008.06.007
  - Ragon, T. (2024). Deepgem-egf [software]. Retrieved from https://github.com/thearagon/DeepGEM\_EGF doi: 10.5281/zenodo.14472786
  - Ross, Z. E., Cochran, E. S., Trugman, D. T., & Smith, J. D. (2020). 3D fault architecture controls the dynamism of earthquake swarms. Science, 368(6497), 1357–1361. doi: 10.1126/science.abb0779
  - Ross, Z. E., Kanamori, H., & Hauksson, E. (2017). Anomalously large complete stress drop during the 2016 Mw 5.2 Borrego Springs earthquake inferred by waveform modeling and near-source aftershock deficit. Geophysical Research Letters, 44(12), 5994–6001. doi: 10.1002/2017GL073338
  - Shearer, P. M., Abercrombie, R. E., Trugman, D. T., & Wang, W. (2019). Comparing EGF Methods for Estimating Corner Frequency and Stress Drop From P Wave Spectra. *Journal of Geophysical Research: Solid Earth*, 124(4), 3966–3986. doi: 10.1029/2018JB016957
  - Shearer, P. M., Prieto, G. A., & Hauksson, E. (2006). Comprehensive analysis of earthquake source spectra in southern California. *Journal of Geophysical Research: Solid Earth*, 111(B6). doi: 10.1029/2005JB003979
  - Sun, H., & Bouman, K. L. (2021). Deep Probabilistic Imaging: Uncertainty Quantification and Multi-modal Solution Characterization for Computational Imaging. In *The Astrophysical Journal*. doi: 10.48550/arXiv.2010.14462
  - Sun, H., Bouman, K. L., Tiede, P., Wang, J. J., Blunt, S., & Mawet, D. (2022). α-deep Probabilistic Inference (α-DPI): Efficient Uncertainty Quantification from Exoplanet Astrometry to Black Hole Feature Extraction. The Astrophysical Journal, 932(2), 99. doi: 10.3847/1538-4357/ac6be9
  - Supino, M., Festa, G., & Zollo, A. (2019). A probabilistic method for the estimation of earthquake source parameters from spectral inversion: application to the 2016–2017 Central Italy seismic sequence. *Geophysical Journal International*, 218(2), 988–1007. doi: 10.1093/gji/ggz206
  - Thomson, D. (1982). Spectrum estimation and harmonic analysis. *Proceedings of the IEEE*, 70(9), 1055–1096. doi: 10.1109/PROC.1982.12433
  - Törnman, W., Martinsson, J., & Dineva, S. (2021). Robust Bayesian estimator for S-wave spectra, using a combined empirical Green's function. *Geophysical Journal International*, 227(1), 403–438. doi: 10.1093/gji/ggab184
  - Trugman, D. T. (2022). Resolving Differences in the Rupture Properties of M5 Earthquakes in California Using Bayesian Source Spectral Analysis. *Journal of Geophysical Research: Solid Earth*, 127(4), e2021JB023526. doi: 10.1029/2021JB023526
  - Trugman, D. T., & Shearer, P. M. (2017). Application of an improved spectral decomposition method to examine earthquake source scaling in Southern California. *Journal of Geophysical Research: Solid Earth*, 122(4), 2890–2910. doi: 10.1002/2017JB013971
  - UC Santa Barbara. (1989). UC Santa Barbara Engineering Seismology Network. International Federation of Digital Seismograph Networks. doi: 10.7914/SN/SB
  - Vallée, M. (2004). Stabilizing the Empirical Green Function Analysis: Development of the Projected Landweber Method. Bulletin of the Seismological Soci-

ety of America, 94(2), 394–409. doi: 10.1785/0120030017

- Vallée, M., Charléty, J., Ferreira, A. M. G., Delouis, B., & Vergoz, J. (2011). SCARDEC: a new technique for the rapid determination of seismic moment magnitude, focal mechanism and source time functions for large earthquakes using body-wave deconvolution. Geophysical Journal International, 184(1), 338–358. doi: 10.1111/j.1365-246X.2010.04836.x
  - Vallée, M., & Douet, V. (2016). A new database of source time functions (STFs) extracted from the SCARDEC method. *Physics of the Earth and Planetary Interiors*, 257, 149–157. doi: 10.1016/j.pepi.2016.05.012
  - Van Houtte, C., & Denolle, M. (2018). Improved Model Fitting for the Empirical Green's Function Approach Using Hierarchical Models. *Journal of Geophysical Research: Solid Earth*, 123(4), 2923–2942. doi: 10.1002/2017JB014943
  - Vernon, F. (1982). ANZA Regional Network. International Federation of Digital Seismograph Networks. doi: 10.7914/SN/AZ
  - Viegas, G., Abercrombie, R. E., & Kim, W.-Y. (2010). The 2002 M5 Au Sable Forks, NY, earthquake sequence: Source scaling relationships and energy budget. *Journal of Geophysical Research: Solid Earth*, 115(B7). doi: 10.1029/2009JB006799
  - Viesca, R. C., & Garagash, D. I. (2015). Ubiquitous weakening of faults due to thermal pressurization. *Nature Geoscience*, 8(11), 875–879. doi: 10.1038/ngeo2554
- Yano, T. E., Shao, G., Liu, Q., Ji, C., & Archuleta, R. J. (2014). Coseismic and potential early afterslip distribution of the 2009 Mw 6.3 L'Aquila, Italy earthquake. *Geophysical Journal International*, 199(1), 23–40. doi: 10.1093/gji/ggu241